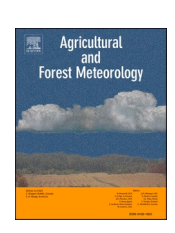
ELSEVIER

Contents lists available at ScienceDirect

Agricultural and Forest Meteorology

journal homepage: www.elsevier.com/locate/agrformet





Isotopic partitioning of evapotranspiration in a mesic grassland during two wetting–drying episodes

Xiangmin Sun^{a,*}, Bradford P. Wilcox^a, Chris B. Zou^b, Elaine Stebler^b, Jason B. West^a, Briana Wyatt^c

- ^a Department of Ecosystem Science and Management, Texas A&M University, College Station, TX, 77843, USA
- b Department of Natural Resource Ecology and Management, Oklahoma State University, Stillwater, OK, 74078, USA
- ^c Department of Plant and Soil Sciences, Oklahoma State University, Stillwater, OK, 74078, USA

ARTICLE INFO

Original content: sun, xiangmin (2020), for Isotopic ET evapotranspiration in Tallgrass Prairie, Mendeley Data, v1, 2015, https://doi.org/10.17632/4vpjkxs4wx.1

Keywords:
Evapotranspiration partitioning
Tallgrass prairie
Plant transpiration
Precipitation
Water stable isotopes
Vapor pressure deficit

ABSTRACT

Evapotranspiration (*ET*) is the dominant water loss flux in mesic tallgrass prairie. Partitioning of *ET* into its two components—soil evaporation (*E*) and plant transpiration (*T*)—is challenging but critical for unraveling biophysical processes underlying ecosystem functioning and sustainability in a changing environment. Because of the pulsed nature of ecophysiological processes in this water-limited ecosystem, we carried out two field campaigns during wetting–drying episodes following precipitation pulses. We applied a two-source isotopic mixing model for *ET* partitioning. The isotopic compositions of *ET*, *E*, and $T(\delta_{ET}, \delta_{E}, \text{ and } \delta_{T})$ were determined by the Keeling-plot method, the Craig–Gordon model, and midday plant xylem water, respectively. We found that the *ET* partitioning results (T/ET) could be more accurately quantified with ^{2}H than with ^{18}O 0, because of (1) the better performance of ^{2}H in Keeling-plot regressions of high-temporal-frequency isotopic measurements of water vapor, and (2) the stronger sensitivity of ^{2}H to the equilibrium fractionation. Using ^{2}H values, we found that the mean \pm standard deviation of T/ET was 0.84 ± 0.05 and 0.92 ± 0.06 during two field campaigns. Soil water near the surface (especially the top 10 cm) responded actively during these two wetting–drying episodes and was the major source for the total *ET* flux during the initial drying periods. Only after shallow soil moisture had become substantially exhausted did deeper soil layers (up to 1 m) increasingly become the major source for the *T* flux, while the *E* flux declined progressively to a negligible level.

1. Introduction

The tallgrass prairie in the Great Plains of North America is an important but endangered ecosystem. This mesic grassland is characterized by high biodiversity (Chapman et al., 1990; Steinauer and Collins, 1996), and is central to agronomical development and biodiversity conservation (Freese et al., 2014). As a result of historical agricultural conversion (Samson et al., 2004) and recent woody plant encroachment (Archer et al., 2017; McKinley and Blair, 2008; Zou et al., 2014), the tallgrass prairie is now designated as an endangered ecosystem. Understanding the ecohydrological processes occurring in this ecosystem is fundamental for evaluating the ecophysiological properties and sustainability of this endangered ecosystem under land use/cover change and climate change (Knapp et al., 2008; Shafer et al., 2014).

A clear understanding of ecohydrological processes in water-limited ecosystems demands accurate quantification of evapotranspiration (*ET*) and its partitioning (Kool et al., 2014; Newman et al., 2006; Sutanto et al., 2014). Evapotranspiration is the largest water-loss flux in tallgrass prairie (Sun et al., 2019a; Wagle et al., 2017; Zou et al., 2014). The *ET* flux consists of soil evaporation (*E*) along the soil–atmosphere continuum, plant transpiration (*T*) along the soil–plant–atmosphere continuum, and direct evaporation of water intercepted by the plant canopy (*I*). These three components differ in their pathways, temporal dynamics, and water use is inexorably coupled with ecosystem productivity (Good et al., 2015), *ET* partitioning is critical for quantifying biological water demand (Newman et al., 2006) and water-use efficiency (Zhou et al., 2016), and thus has important implications for predicting ecosystem functioning and sustainability in the context of a changing

https://data.mendeley.com/datasets/4vpjkxs4wx/1 DOI: 10.17632/4vpjkxs4wx.1.

* Corresponding author.

E-mail address: sunxm03@tamu.edu (X. Sun).

environment (Fisher et al., 2017). The results of ET partitioning are usually expressed as the ratio T/ET, representing the role of plant physiological processes in the hydrologic cycle.

Soil water availability, as a key link between hydrologic and ecological processes, strongly controls the dynamics of ET partitioning in water-limited ecosystems. Recharged by infiltrated precipitation, soil water supplies both E and T fluxes; E depletes soil water near the surface while T withdraws water across the active rooting zone (Scanlon and Kustas, 2010). No obvious effect of total precipitation on *T/ET* has been found at the annual or the growing-season scale (Berkelhammer et al., 2016; Fatichi and Pappas, 2017; Gu et al., 2018; Li et al., 2019; Schlesinger and Jasechko, 2014). Besides long-term (seasonal, annual, and interannual) variations, soil moisture varies over the short term (sub-daily, daily, weekly) due to highly stochastic precipitation inputs (Knapp et al., 2008; Newman et al., 2006) and strong atmospheric water demand. Thus, ET partitioning during these dynamic wetting-drying episodes following individual water pulses warrants more attention for a mechanistic understanding of water diffusion from terrestrial ecosystems to the atmosphere. A few short-term studies have investigated ET partitioning in water-limited regions-e.g., grasslands (Good et al., 2014; Yepez et al., 2005) and winter wheat (Aouade et al., 2016) following irrigation. But to our knowledge, no such study has been carried out in the tallgrass prairie grassland.

Measuring E and T fluxes separately is methodologically challenging (Brooks, 2015). For this reason, the isotopic two-source mixing model, which is based on the fact that the isotopic composition of soil-evaporation water vapor is distinct from that of plant transpiration, has become an indispensable tool for ET partitioning (Sun et al., 2019b; Sutanto et al., 2014; Wang and Yakir, 2000; Zhang et al., 2010). Because one isotope is sufficient for solving the two-source mixing model, most studies on ET partitioning used only one isotope: either ²H (Good et al., 2014; Wang et al., 2013; Wang et al., 2010; Yepez et al., 2005) or ¹⁸O (Dubbert et al., 2014; Hu et al., 2014; Wang and Yakir, 2000; Wen et al., 2016; Zhang et al., 2018). Only a few studies have reported different results from the use of ²H and ¹⁸O in parallel (Gaj et al., 2016; Quade et al., 2019; Xu et al., 2008; Yepez et al., 2003). In addition, the criteria for selecting one isotope over the other (e.g., the applicability and uncertainties associated with each) have not been thoroughly investigated and evaluated.

The overarching goal of our study is to present the short-term dynamics of ET partitioning following precipitation events when this tallgrass prairie is approaching the peak growing season. Using the isotopic approach (both $^2\mathrm{H}$ and $^{18}\mathrm{O}$), we investigated ET partitioning during two drying episodes characterized by a contrast in soil moisture profiles. Our objectives are

- to compare the performance of ²H with that of ¹⁸O for isotopic *ET* partitioning;
- to determine the pattern of daily T/ET during the two drying episodes:
- to investigate the effects on the temporal pattern of ET partitioning of

 (a) soil water availability at different depths and (b) atmospheric processes.

2. Materials and methods

Our study consisted of two intensive field campaigns at a grassland site in a tallgrass prairie ecosystem. An eddy covariance (EC) system, coupled with various biometeorological sensors, was set up to measure the bulk ET flux, atmospheric processes, and soil hydrothermal properties. Near the EC system, we also sampled waters from various ecohydrological pools for isotopic analysis. We assumed the same contributing footprint for the EC measurement as for the isotopic sampling of atmospheric water vapor. All the measurements were recorded in local time (LT = UTC - 6 H), disregarding daylight-saving time. All isotopic data were reported in δ -notation as per mil units (‰), namely,

as concentration ratios related to the Vienna Standard Mean Ocean Water (VSMOW).

2.1. Study site

This study was conducted at the Range Research Station (36°3′24.6″N, 97°11′28.3″W, elevation about 330 m above sea level) of Oklahoma State University, located in north-central Oklahoma, USA (Fig. 1). Long-term climate data (1997–2016) from the nearby Marena weather station (1.9 km away) show a subhumid climate, with an average air temperature of 15.63 \pm 0.83°C (mean \pm standard deviation; all mean values are expressed this way unless otherwise specified) and mean annual precipitation of 875 \pm 206 mm (see Figs. S1 and S2 in the Supplementary materials).

The terrain is mostly flat, with slopes ranging from 1% to 8%, and the soil type is a mosaic of Coyle loam and Stephenville–Darnell complex (https://websoilsurvey.sc.egov.usda.gov/). Our analysis showed a loamy soil texture for the top 15-cm layer at our site. The grassland is dominated by perennial, warm-season (C₄) grasses, including little bluestem (*Schizachyrium scoparium*} [Michx.] Nash), big bluestem (*Andropogon gerardii* Vitman), Indiangrass (*Sorghastrum nutans* [L.] Nash), switchgrass (*Panicum virgatum* L.), and tall dropseed (*Sporobolus asper* [Michx.] Kunth) (Limb et al., 2010).

2.2. Micro-meteorological measurements

An eddy covariance (EC) system with a standard suite of biometeorological sensors was installed to measure the energy and mass exchange between the ground surface and atmosphere (Fig. 1). An integrated $\rm CO_2$ and $\rm H_2O$ open-path gas analyzer and a three-dimensional sonic anemometer (EC100, IRGASON, Campbell Scientific Inc., Logan, Utah) were mounted 3 m above the ground for high-frequency measurement of turbulence fluxes. Low-frequency measurements include net radiation

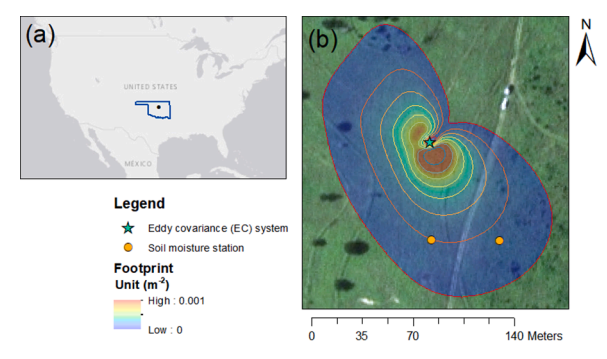




Fig. 1. Map of the study site. (a) Location of the study site in Oklahoma; (b) the footprint climatology for eddy covariance measurements (reprinted from Sun et al., (2019a) with permission); (c) 3-m tower equipped with the eddy covariance system and the WS-CRDS analyzer (in the vehicle) for *in situ* sampling of water vapor.

 (R_n) , air temperature (T_{air}) , and relative humidity (h_{air}) at this height. The average soil temperature (T_{soil}) for the layer above 8 cm was measured with an averaging soil thermocouple (TCAV, Campbell Scientific Inc., Logan, Utah). Above-canopy precipitation (P) was also recorded. Detailed information on the configuration of these measurement devices and on data processing are described in Sun et al. (2019a).

In close proximity to the EC tower, an array of additional biometeorological sensors were installed on a steel post: a photo-synthetically active radiation (PAR) sensor (model QSO-S, Decagon Devices Inc., Pullman, WA) for measuring photosynthetic photon flux density (*PPFD*) above the plant canopy (mmol m $^{-2}$ s $^{-1}$) at approximately 1.5 m; a pair of spectral reflectance sensors (SRS, Decagon Devices Inc., Pullman, WA) for measuring the Normalized Difference Vegetation Index (*NDVI*); and a leaf wetness sensor (model LWS, Decagon Devices Inc., Pullman, WA), positioned 30 cm above the leaf surface and at an angle of 45° to the horizontal. Data from these sensors were stored in a datalogger (EM50, Decagon Devices Inc., Pullman, WA) with a frequency of 5 min, from which 30-min averages were subsequently calculated. In addition, the leaf area index (*LAI*) was recorded with a line ceptometer (AccuPAR LP-80, Decagon Devices Inc., Pullman, WA) along three transects under direct solar radiation on July 29, 2016.

2.3. Soil moisture dynamics and soil hydraulic parameters

Two soil-moisture stations were established within the footprint of the EC tower (Fig. 1b) to measure the volumetric soil water content (θ_{soil}). Probes (ECH₂O EC-5, Decagon, Pullman, WA) were inserted at depths of 5, 20, 45, and 80 cm for four depth intervals across the profile: 0–10 cm, 10–30 cm, 30–60 cm, and 60–100 cm (Fig. 1). For each depth interval (i, 1–4), we calculated daily changes in soil water storage ($\Delta S_i = \Delta \theta_i \times z_i$, mm day $^{-1}$), where, for layer i, $\Delta \theta_i$ is the variation in θ during a rain-free day (calculated as the difference between the first and the last observation in daily records), and z_i is the depth increment (10 cm, 20 cm, 30 cm, and 40 cm, respectively).

Close to these soil-moisture stations, soil samples were collected with coil from three depth intervals (0–5 cm, 5–10 cm, and 10–15 cm) for analysis of soil texture and soil water retention properties, including

volumetric water content at field capacity (-33 kPa, m³ m⁻³) and permanent wilting point (-1500 kPa, m³ m⁻³). These data were used as inputs for the Rosetta pedotransfer function (Schaap et al., 2001) to enable estimation of soil hydraulic parameters—such as residual water content (θ_{res}) and saturation water content (θ_{sat}), both measured in m³ m⁻³.

2.4. Isotopic sampling

During the peak growing season, we carried out two intensive field campaigns following precipitation events. Isotopic sampling was done at two-day intervals during Campaign 1 (June 4–12, 2016), and at daily intervals for Campaign 2 (June 27–30, 2016). Within each day, sampling lasted throughout most of the daylight hours and consisted of sampling waters of different ecohydrological pools (atmospheric vapor in the ecosystem boundary layer, bulk leaf and root xylems of grasses, and shallow soil layers) for analysis. The only exceptions were June 4 and June 27, when for logistic reasons measurements began at 13:30. Additionally, throughout 2016 we collected precipitation samples following rainfall events at the campus of Oklahoma State University (11 km from the study site).

2.4.1. Sampling of atmospheric water vapor

To determine the isotopic composition of atmospheric water vapor (δ_V) , we employed an *in situ* high-temporal-resolution (about 0.13 Hz) sampling apparatus (Fig. 2). Air samples were continuously drawn off through Gelman 1-µm filters (part # 9967-008, LI-COR, Nebraska) at three inlets (at heights of 1 m, 2 m, and 3 m on the EC mast). The system uses a computer-controlled, multiport rotary valve (EMT2SC10MWE, VICI, Houston, Texas) configured to draw an air sample into the measuring system from each of the three inlets in turn, while air from the other two inlets was pumped out as mixed exhaust via the common outlet. This bypass configuration was designed to ensure the "freshness" of the air samples from all inlets. A diaphragm pump (part #286-04198, LI-COR, Lincoln, Nebraska) was employed to remove the mixed exhaust at a flow rate of $< 3.5 \, \text{L} \, \text{min}^{-1}$. Next, each selected air sample was routed to the sampling system for 9 min. During a switch between two heights,

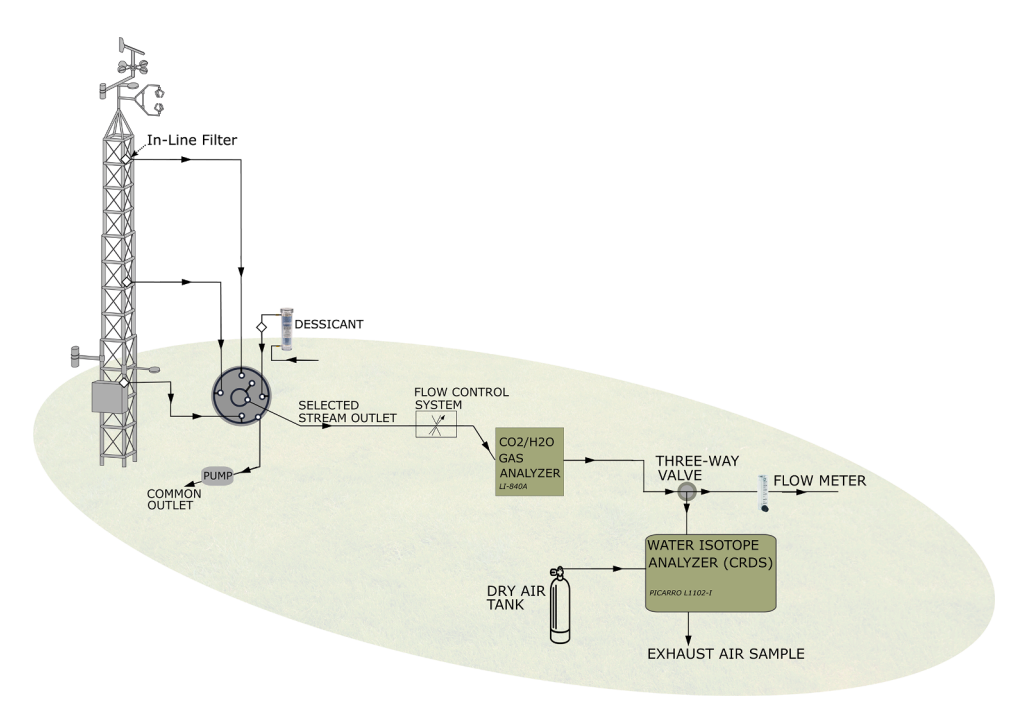


Fig. 2. Schematic of the field set-up for measuring the isotopic composition of atmospheric water vapor, including an automatic valve for switching among sources of water vapor from different heights, a water vapor concentration analyzer used for calibration, and the WS-CRDS analyzer. The three inlets for this sampling system are positioned on the eddy covariance mast.

air samples from a desiccant column were interposed for 1 min as a separation signal to label air samples from different heights. The temporal pattern of δ_V sampling is illustrated in the Supplementary materials (Fig. S3). Thus, each three-level sampling cycle took 30 min, corresponding to the 30-min interval of ET data obtained from the EC system.

Each selected air sample was then drawn through a flow control unit (LI-670, LI-COR, Lincoln, Nebraska) to an infrared gas analyzer (Li840A, LI-COR, Lincoln, Nebraska). The air sample was then split via a three-way valve and fed into the water isotope analyzer, an infrared wavelength-scanned cavity ring-down spectrometer (L1102-i, WS-CRDS, Picarro Inc., Santa Clara, California), at a rate of $<0.4\ L\ min^{-1}$ under one standard atmosphere.

High-density polytetrafluoroethylene (PTFE) tubing (1/8-inch outer diameter, 1/16-inch inner diameter) was used for this sampling system, because of its minimal memory effect (Sturm and Knohl, 2010) and its high thermal stability. To minimize wind distortion for the EC measurements, the sampling apparatus was placed about 8 m downwind along the prevailing wind direction (Fig. 1). We selected two liquid working standards encompassing the ranges of δ_V : one with a $\delta^2 H$ of -7.13 \pm 0.75 % and a $\delta^{18} O$ of -6.76 \pm 0.06 %, and the other with a $\delta^2 H$ of -213.84 \pm 0.48 % and a $\delta^{18} O$ of -28.11 \pm 0.11 %. Each standard was used in the field on alternate days, in the late afternoon following δ_V observation, when the WS-CRDS analyzer switched to liquid mode with the evaporator turned on. About eight analyses were done per day, and only the last 4 results were used for drift correction and quality assurance. The purge carrier gas used in calibration was supplied by a high-pressure, zero-air gas cylinder.

The WS-CRDS analyzer measured the mixing ratio (w in mmol mol^{-1}) and δ_V of atmospheric water vapor. We selected the middle 6min data from the 10-min interval for each height because the wsignal reached stability in two minutes after the switch from one inlet to the next (see Figs. S3 and S4 in the Supplementary materials). The w values from the WS-CRDS analyzer were crosschecked and calibrated by the parallel results of the online gas analyzer (Li840A). The δ_V data were corrected and calibrated in four steps: (1) for each 30-min interval, outliers having values two standard deviations or more from mean values (accounting for approximately 8.5%) were removed; (2) water vapor concentration effects were corrected (Schmidt et al., 2010) based on the water mixing ratio dependency for international standards (see Supplementary Fig. S5); (3) instrument drift was corrected, and quality assurance was achieved, through in-situ analysis of liquid working standards at the daily interval; and (4) standardization to the international VSMOW-Standard Light Antarctic Precipitation (SLAP) scale through indoor intensive testing of working and international standards before and after the field campaigns. The two working standards were intensively analyzed along with VSMOW-GISP (Greenland Ice Sheet Precipitation)-SLAP standards in the laboratory, usually with 30-40 times of analysis for each standard, for water concentration dependency analysis and scaling of δ_V to VSMOW-SLAP standards. The drift was less than 5% and 0.5% for ²H and ¹⁸O, respectively, and the analytical uncertainty (standard deviation) was less than 1.74 % and 0.17 % for ²H and ¹⁸O, respectively.

2.4.2. Sampling of water in surface soil, vegetation, and precipitation

During the two *in situ* campaigns, we collected soil and plant samples three times each day (morning, noon, and afternoon) for subsequent extraction of water via cryogenic vacuum distillation. Using a shovel, we collected soil samples from the 0- to 15-cm layer, because for loamy soils the effective depth of bare-soil evaporation is usually located within the top 15 cm (Wythers et al., 1999). Another study in a temperate grassland also found that sampling the shallow soil layer within 15 cm in depth is a reasonable approach for δ_E (Hu et al., 2014). To better capture the δ_{soil} at the evaporation front, the upper soil layer (about 3–5 cm in depth), if noticeably dehydrated, was excluded from the mixed soil samples taken

from the 15-cm-depth soil layer. In addition, from areas close to the sampled soils, we collected samples (randomly selected) of the dominant grasses—upper root crowns and whole leaves from the upper canopy. We took samples of the thick, fleshy root crowns because this plant tissue is the least variable and best represents isotopic values of a well-mixed root water uptake from different depths (Barnard et al., 2006; Durand et al., 2007). We did not differentiate between grass species in our sampling because studies of these species in other grasslands found no difference in isotopic composition of the plant-root xylem water (δ_X) (Eggemeyer et al., 2009) and no complementary water use (Bachmann et al., 2015).

All soil and plant samples were quickly transferred into gas-tight, screw-capped 12-mL glass vials (Fisherbrand, catalog # 14-955-310, Pittsburgh, PA), wrapped with Parafilm® M membrane (Bemis Company, Inc., Neenah, WI, USA), and stored in a dark, cool box in the field until they could be transferred to a laboratory refrigerator (4 $^{\circ}\text{C}$) to await vacuum extraction. Because of the large number of samples and the laborious process of cryogenic distillation, we did not collect replicates for soil and plant samples.

2.4.3. Analysis of water samples

Cryogenic vacuum distillation (Ehleringer et al., 2000; West et al., 2006) was used to extract water from the plant and soil samples at the Stable Isotopes for Biosphere Science Laboratory at Texas A&M University. The soil and plant samples were heated under vacuum (< 0.04 hPa) with water baths maintained at 90°C-100°C. The water was evaporated from the sample by immersing the bottom of the tube in the bath, then condensed in a collection tube with its end immersed in a cold trap. The deposited ice sample was melted at room temperature and quickly transferred into a 2-mL vial, which was sealed and stored at 4 °C before isotopic analysis. Any extracted water with a noticeable smell or cloudy appearance was filtered through a 0.22-µm filter (catalog # 09-720-002, Fisherbrand, Fisher Scientific, Pittsburg, PA) before transfer. Within two weeks after extraction, isotopic analysis was carried out with a mass spectrometry (IRMS) system, consisting of a high-temperature reactor ("Temperature Conversion/Elemental Analyzer") coupled on-line to an isotope ratio mass spectrometer (Delta VTM IRMS) via a Conflo IV interface (all components from Thermo Fisher Scientific, Bremen, Germany). The analyzed results from this IRMS system were considered not affected by organic contaminants (spectral contamination by organic substances in plants could be a serious concern for laser spectrometer analysis (Penna et al., 2018; West et al., 2010; West et al., 2011)). Each batch of 30-40 samples was calibrated against in-house water standards: SIBS-wA ($\delta^2 H = -390.8 \pm$ 1.6 %, $\delta^{18}\text{O} = -50.09 \pm 0.33 \text{ }\%$) and SIBS-wP ($\delta^2\text{H} = -34.1 \pm 1.9 \text{ }\%$, $\delta^{18}O = -4.60 \pm 0.24$ %) (Adams et al., 2020). Quality control was performed using an in-house water standard, SIBS-wU ($\delta^2 H = -120.2 \pm$ 1.5 %, $\delta^{18}O = -15.95 \pm 0.27$ %), and the standard deviation for our samples was 1.3% for 2 H and 0.14% for 18 O. These in-house standards were calibrated and scaled to VSMOW-GISP-SLAP standards.

The precipitation samples were analyzed for isotopic composition (δ_P) by means of the WS-CRDS analyzer in liquid mode. The two *in-situ* working standards used in calibrating the WS-CRDS analyzer during field campaigns were verified by the IRMS analyzer for cross-checking isotopic measurements of water vapor and precipitation samples obtained by laser spectroscopy and those of extracted liquid water obtained by mass spectroscopy.

3. The isotopic two-source mixing model for ET partitioning

The isotopic approach works on the principle that strong fractionation processes are involved in soil evaporation, but usually not in the uptake of water by plant roots during transpiration (Bowen et al., 2019; Gat, 1996; Yakir and Sternberg, 2000). If evaporation of water intercepted by the canopy is not taken into account, the isotopic compositions of bulk ET and of its two constituents (i.e., δ_{ET} , δ_{E} , and δ_{ET}) can be

used to estimate T/ET via a simple, two-source linear mixing model:

$$\frac{T}{ET} = \frac{\delta_{ET} - \delta_E}{\delta_T - \delta_F}.\tag{1}$$

Of the terms in Eq. 1, only δ_{ET} can be estimated via isotopic sampling of atmospheric water vapor (using a field-deployable laser spectrometer, such as the WS-CRDS analyzer). The values of δ_E and δ_T are usually calculated based on isotopic sampling of liquid water extracted from soil samples and plant xylem. We obtained daily values of δ_{ET} and δ_E based on weights carried by the ET flux and the VPD variable, respectively. The errors in δ_{ET} and δ_E were propagated accordingly. The daily δ_T value and its error were approximated by midday δ_X and its analysis error, respectively. Coupled with daily T/ET analysis (Eq. 1), the bulk ET flux measured by EC was used to calculate the individual fluxes of E and E at the daily scale as well.

3.1. δ_{ET} via the Keeling-plot method

The value of δ_{ET} from a terrestrial ecosystem is usually distinct from the isotopic composition of the ambient background air (δ_{bg}) above. The linear mixing of upward ET and background air creates a gradient in δ_V in the turbulent boundary layer (Xiao et al., 2018). This gradient can be used to extrapolate δ_{ET} via the Keeling-plot method, a mass balance mixing equation (Keeling, 1958):

$$\delta_V = \omega_{bg} \left(\delta_{bg} - \delta_{ET} \right) \frac{1}{\omega} + \delta_{ET}, \tag{2}$$

where $\omega_{\rm bg}$ and ω stand for mixing ratios for the background air and the boundary layer, respectively.

Two assumptions are involved: (1) that the values of ω_{bg} , δ_{bg} , and δ_{ET} —namely, the slope parameter in Eq. 2—remain constant during the analysis period (Wu et al., 2017); and (2) that water vapor losses come only from turbulent mixing between the two source layers, and not from other factors (e.g., condensation). In other words, turbulent mixing is the only process in the upward transport of water vapor (Quade et al., 2019; Yakir and Sternberg, 2000).

To meet the first assumption, we applied the Keeling-plot method at hourly intervals (the sample size was about 235 ± 71 points), because this method is more robust at shorter time intervals (Good et al., 2012). To better meet the second assumption, δ_V was obtained from three heights (see Section 2.4.1) close to the vegetation canopy, where disturbance from advection is minimal (Lee et al., 2006; Xiao et al., 2018). We used the ordinary least squares regression (OLS) method to apply the Keeling-plot analysis, which is illustrated in the Supplementary materials (Figs. S6 and S7).

3.2. δ_E via the Craig-Gordon model

We quantified δ_E with the popular Craig–Gordon model, which takes into account both equilibrium fractionation (α_{eq}) at the liquid–vapor interface and kinetic fractionation (α_k) along the laminar diffusion layer below the "free" atmosphere (Craig and Gordon, 1965; Dubbert et al., 2013; Horita et al., 2008). The Craig–Gordon equation is:

$$\delta_E = \frac{\frac{\delta_{Se}}{a_{eq}} - h\delta_a - \varepsilon_k - \varepsilon_{eq}}{1 - h + \varepsilon_k},\tag{3}$$

where δ_{Se} is the isotopic composition of liquid soil water at the evaporation front (approximated by δ_{soil} of the upper 15-cm depth interval in this study), and δ_a is the isotopic value of the free atmospheric water vapor, approximated by δ_V measured by the WS-CRDS analyzer at 1 m.

3.2.1. Equilibrium fractionation at the liquid-vapor interface

The value of α_{eq} (> 1) at the liquid–vapor interface was calculated as a function of soil temperature (T_{soil}' in K) at the evaporation front (Cappa

et al., 2003; Majoube, 1971), as follows:

for
$${}^{2}\text{H}$$
, $10^{3}\ln\alpha_{eq} = 24.844 \left(\frac{10^{6}}{T_{col}^{-2}}\right) - 76.248 \left(\frac{10^{3}}{T_{coll}^{-2}}\right) + 52.612$, (4a)

for ¹⁸O,
$$10^3 \ln \alpha_{eq} = 1.137 \left(\frac{10^6}{T_{soil}^{-2}} \right) - 0.4156 \left(\frac{10^3}{T_{soil}} \right) + 2.0667.$$
 (4b)

These robust empirical relationships (Eqs. 4a and 4b) are still widely used after almost five decades (Horita et al., 2008; Soderberg et al., 2012; Xiao et al., 2018). The deviation of α_{eq} from unity, ε_{eq} , can be defined as $\varepsilon_{eq} = (\alpha_{eq} - 1) \times 10^3$ %.

3.2.2. Kinetic fractionation within the diffusion layer

As the only parameter in Eq. 3 that is not obtainable from field measurement, ε_k —the deviation of α_k from unity—can be calculated as follows (Craig, 1961; Horita et al., 2008):

$$\varepsilon_k = (1 - h) \frac{r_M}{r} \left[1 - \left(\frac{D_i}{D} \right)^n \right]. \tag{5}$$

We assumed the "weighting term" $(\frac{T_M}{r})$ in Eq. 5 as unity because the atmospheric boundary layer was not strongly perturbed by the soil evaporation efflux. The dominating factor for variability in ε_k is relative humidity (h), which was normalized to the soil temperature $(T_{soil}$ in °C) at the evaporation front (Craig and Gordon, 1965; Horita et al., 2008; Soderberg et al., 2012) using the empirical Tetens equation (Buck, 1981; Tetens, 1930), as follows:

$$h = h_{air} \exp\left(\frac{17.502 \ T_{air}}{240.97 + T_{air}} - \frac{17.502 \ T_{soil}}{240.97 + T_{soil}}\right),\tag{6}$$

where h_{air} is the relative humidity of the ambient air, and T_{air} is the ambient air temperature (°C). Both variables were obtained from the EC system (section 2.2).

The diffusivity ratio of water isotopologues ($\frac{D}{D}$ in Eq. 5) along the laminar layer above the interface is 0.9755 for 2H and 0.9723 for ^{18}O (Merlivat, 1978). This ratio can be reduced when the turbulent mixing layer above the laminar layer interacts strongly with the evaporation surface (Soderberg et al., 2012). The aerodynamic parameter n in Eq. 5 incorporates the development of laminar flow as volumetric soil water content (θ) changes (Braud et al., 2005a; Braud et al., 2005b; Good et al., 2012; Mathieu and Bariac, 1996), as follows:

$$n = \frac{0.5 (\theta_{soil} - \theta_{res}) + (\theta_{sat} - \theta_{soil})}{\theta_{sat} - \theta_{res}},$$
(7)

where θ_{soil} , θ_{res} , and θ_{sat} are, respectively, the observed, residual, and saturated values of θ at the evaporation front. We obtained θ_{res} and θ_{sat} from soil water retention properties analysis (Section 2.3) based on two sampled 15-cm soil columns. We approximated θ_{soil} from the soil water content of the 0- to 10- cm depth interval (average of measured values from the two moisture stations). Here and elsewhere in this paper, δ , ε_{eq} , and ε_k are applicable to both 2 H and 18 O unless otherwise specified.

3.3. δ_T under the isotopic steady–state assumption

Under the isotopic steady-state (ISS) assumption, the isotopic composition of water transpired via leaf stomata equals that of xylem sap entering the leaf, which can be approximated with δ_X . Because no isotopic fractionation occurs during root water uptake and upward movement of water to the leaves (Brunel et al., 1997; Wang and Yakir, 2000), we were able to use δ_X to approximate daily δ_T in the early afternoon (13:00–15:00)—when, with the stomata fully open, the ISS assumption can be met (Sutanto et al., 2014). Although the isotopic non-steady-state condition could be more accurate for sub-daily analysis in a highly variable environment or for plants with long leaf-water

turnover times (Lai et al., 2006; Yepez et al., 2005), ISS can be used to approximate integrated daily δ_T (Dubbert et al., 2014; Lai et al., 2006; Wang et al., 2015)—especially for grasses, in which leaf-water turnover time is short (Yakir and Sternberg, 2000).

3.4. Uncertainty in evapotranspiration partitioning

According to Eq. 1, the uncertainty in daily T/ET results is derived from uncertainties in δ_E , δ_T , and δ_{ET} . Because all three of these values were measured independently, the variance of T/ET ($\sigma_{T/ET}^2$) can be calculated as follows (Phillips and Gregg, 2001):

$$\sigma_{T/ET}^2 = \frac{1}{(\overline{\delta_T} - \overline{\delta_E})^2} \left[\sigma_{\delta_{ET}}^2 + \left(\frac{T}{ET} \right)^2 \sigma_{\delta_T}^2 + \left(1 - \frac{T}{ET} \right)^2 \sigma_{\delta_E}^2 \right], \tag{8}$$

where $\overline{\delta_E}$ and $\overline{\delta_T}$ are daily mean values, and $\sigma_{\delta_ET}^2$, $\sigma_{\delta_E}^2$, and $\sigma_{\delta_T}^2$ are the daily variances of δ_{ET} , δ_E , and δ_T , respectively. According to Eq. 8, $\sigma_{T/ET}^2$ is not only inversely proportional to the difference between $\overline{\delta_T}$ and $\overline{\delta_E}$, but is also proportional to $\sigma_{\delta_ET}^2$, $\sigma_{\delta_E}^2$, and $\sigma_{\delta_T}^2$, and these three variables depend on the analytical precision of the isotopic analyzer and/or the errors involved in the sampling and vacuum distillation procedures (Rothfuss and Javaux, 2017). Since only one xylem sample, taken at midday, was used for daily δ_T estimation, the standard error for δ_T was approximated by using the standard deviation of the sample analysis. In accordance with Eq. 3, we propagated measurement uncertainties in δ_{Se} and δ_a to σ_{δ_E} . Given the lack of replication in field sampling, this study did not take into account the uncertainty related to spatial heterogeneity; in addition, our discrete sampling protocol did not allow for diurnal temporal dynamics in δ_E and δ_T . For this reason, our uncertainty analysis likely underestimates $\sigma_{T/ET}$.

4. Results

4.1. Site environmental conditions

The year 2016 witnessed high variable atmospheric processes (Fig. S2) and a relatively low annual precipitation of 721 mm (18% lower than the long-term mean). June precipitation in 2016, at 47 mm, was the lowest recorded during the past 20 years (Fig. S3). The *LAI* measured on July 29, 2016 ranged between 3.75 and 5.40 m 2 m $^{-2}$. The daily mean *NDVI* values were consistently high during the two field campaigns, ranging between 0.62 and 0.64. Short-term weather and soil moisture conditions during the field campaigns were mostly controlled by precipitation and solar radiation (Fig. 3).

4.1.1. Weather conditions and atmospheric processes

Very little rainfall (< 0.25 mm day $^{-1}$) occurred during the two field campaigns. Measured rainfall prior to Campaign 1 (between May 29 and June 3) was 25 mm; and prior to Campaign 2, a single event (on June 26) was 13 mm (Fig. 3a). These precipitation pulses induced an instant response and high variations in the leaf wetness ratio (LWR, the duration time of leaf wetness as a percentage of a 24-hour period) (Fig. 3b). During our sampling days, except for June 30, leaf wetness (caused by dew or minor night precipitation) was mostly observed during predawn and early morning hours (usually before 09:00). No leaf wetness was noted during our *in-situ* observations. For this reason, we did not consider evaporation from canopy interception (I) as a factor in our I/EI analysis.

The values of R_n and *PPFD* were consistently high during Campaign 1 but showed substantial day-to-day variations during Campaign 2—especially the low R_n reading on June 27 (Fig. 3c). The air temperature (T_{air} , at 3 m) and the surface soil temperature (T_{soil} , in the top 8 cm), both heated by solar radiation, showed similar trends—with T_{soil}

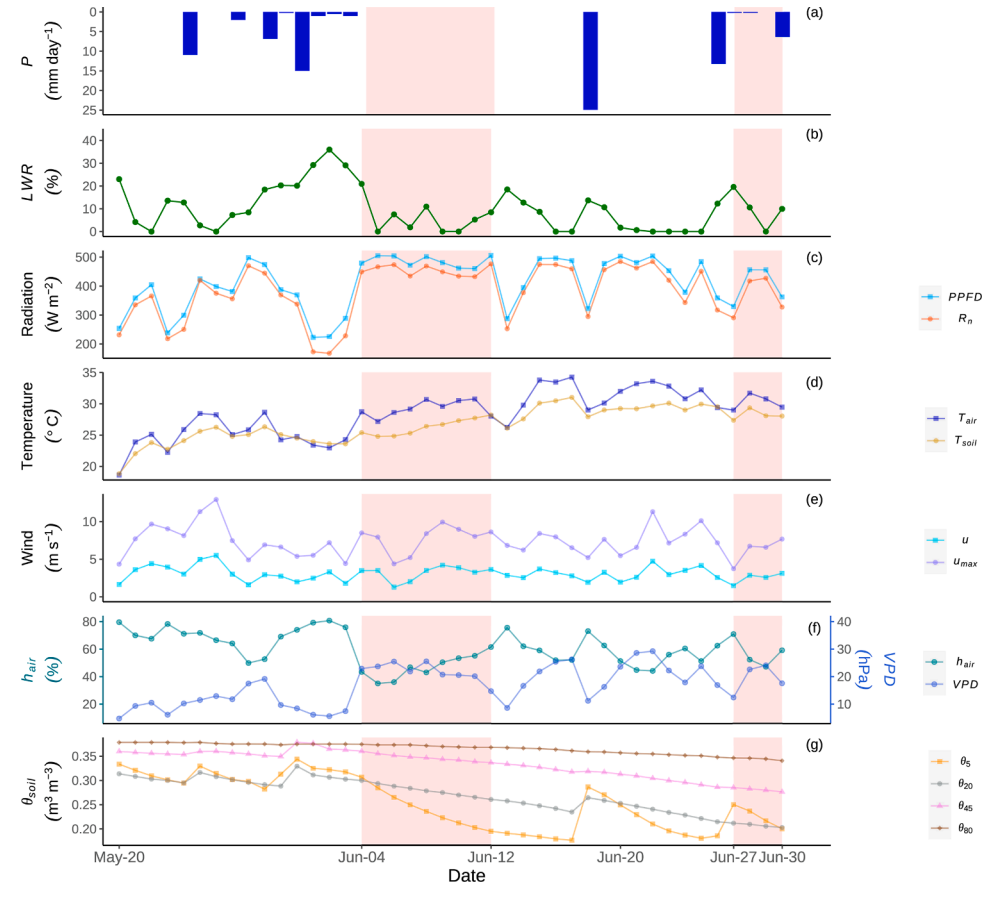


Fig. 3. In situ environmental conditions observed from late May to late June 2016. Except for P and LWR, which were calculated at 24-hour intervals, each point represents the daytime mean value between 09:00 and 19:00 for the corresponding variable. Values for net radiation (R_n) , air temperature (T_{air}) , wind speed (mean value u and maximum value u_{max}), atmospheric water content (relative humidity h_{air} and vapor pressure deficit VPD) were obtained from eddy covariance measurements at 3 m. Variables related to soil processes include soil temperature within the top 8-cm layer (T_{soil}) and volumetric soil water content (θ) at various depths. The red-shaded areas represent the two field campaigns.

averaging 2.50 ± 1.38 °C lower than T_{air} (Fig. 3d), owing to the shading effect of the vegetation canopy (demonstrated by high values of *LAI* and *NDVI*). Wind speed was low on June 8 and June 27 and was particularly stagnant on the latter date with a mean maximum speed of 3.72 m day $^{-1}$ (Fig. 3e). During Campaign 1, the clear weather with high solar radiation resulted in relatively stable day-to-day h_{air} and *VPD* (Fig. 3f). In contrast, precipitation on June 27 and June 30, accompanied by low solar radiation, brought about high h_{air} and low *VPD* (especially on June 27).

4.1.2. Soil moisture dynamics

There were substantial differences in soil water availability across the profile between our two field campaigns. The soil profile was considerably drier during Campaign 2 than during Campaign 1, owing to the high ET flux during June (122 mm) driven by the record low precipitation and intense solar radiation (Figs. 3g and 4). Measurements from both campaigns showed that the dynamics of θ_{soil_5cm} were exceptionally responsive to rainfall pulses. For example, the rainfall events that preceded each campaign rapidly and remarkably replenished antecedent θ_{soil} 5cm, but to a lesser extent for Campaign 2. Further, during both campaigns θ_{soil_5cm} showed dramatic variations, indicating rapid depletion of soil moisture in this shallow surface layer. For example, the daily mean value of θ_{soil} 5cm fell from 0.31 m³ m⁻³ on June 4 to 0.20 m³ m⁻³ on June 12. For the deeper soil layers, over the course of each campaign the daily variation in θ_{soil} diminished progressively with depth as drying proceeded. This pattern was consistent for these layers $(\theta_{soil}_{20cm}, \theta_{soil}_{45cm}, \theta_{soil}_{80cm})$. Since the same steady decrease of θ_{soil_20cm} , θ_{soil_45cm} , and θ_{soil_80cm} would have taken place during the interval between the two campaigns, the θ_{soil} profile for Campaign 2 showed a noticeable divergence from that of Campaign 1 (Fig. 4).

4.2. Stable isotopes as tracers

The depletion of heavier isotopes (2 H and 18 O) in the meteoric components of ecohydrological processes (δ_P and δ_V) and the enrichment of heavier isotopes in the evaporative components (δ_{soil} and δ_{leaf}) are illustrated in a dual-isotope plot (Fig. 5). The values of δ^2 H and δ^{18} O are highly correlated (p-value < 0.001) for waters in all these ecohydrological pools. The slope for δ_P , as observed throughout 2016, was lower than those for the long-term local meteoric water line (LMWL) and

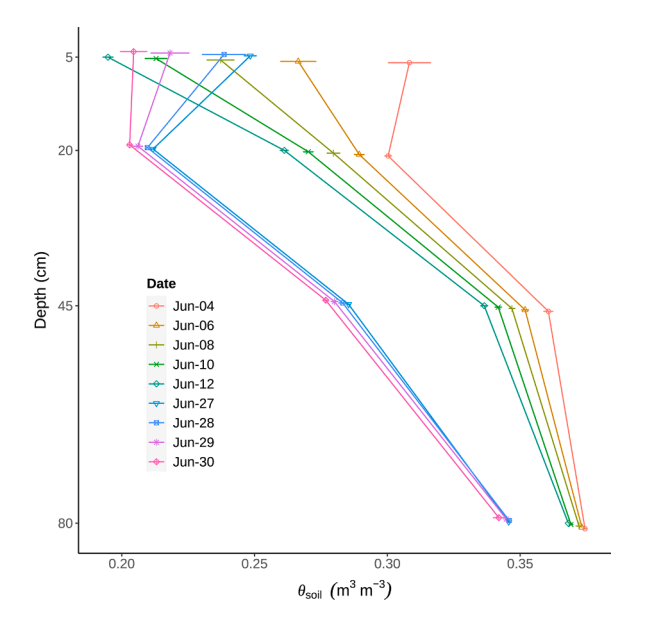


Fig. 4. Temporal variations in the water content (θ_{soil}) profile over the two campaigns. The dots and solid lines are daily means, and error bars represent one standard deviation.

the global meteoric water line (GMWL), which may be attributable to strong below-cloud re-evaporation in this relatively dry year. The values of δ_P showed high storm-to-storm variability during May and June, possibly coinciding with shifts in moisture sources and storm trajectories.

The fact that δ_V (measured within 3 m above the ground) was more negative than δ_P is evidence of isotopic fractionation during the evaporative phase change from liquid to vapor. Because the surface soil layer was strongly recharged by precipitation, the distributions of δ_P and δ_{soil} lie close to each other in the dual-isotope space. But the enrichment of the evaporative component caused δ_{soil} to lie on the right side of δ_P . This soil evaporative fractionation is especially remarkable for δ^{18} O, because kinetic fractionation is greater for $\delta^{18}O$ than for $\delta^{2}H$ (Marshall et al., 2007). Because of the absence of fractionation during most root water uptake (Ehleringer and Dawson, 1992), the distributions of δ_{soil} and δ_X are indistinguishable—and for this reason inter-comparison between δ_{soil} and δ_{X} is often used to infer depths of root water uptake (Rothfuss and Javaux, 2017). The overlapping of δ_X and δ_{soil} suggests that shallow soil moisture is a major source of the water used by plants in this grassland. The strong evaporative enrichment within the leaf stomata is the reason for the considerably heavier isotopic composition of bulk leaf water (δ_{leaf}), and the associated strong kinetic fractionation caused the regression slope for $\delta_{\textit{leaf}}$ to deviate, becoming substantially lower than that for LMWL and δ_P .

The isotopic depletion of atmospheric water vapor and the isotopic enrichment of the evaporative components were further revealed by obtained data series at the diurnal and daily temporal scales (Fig. 6). At the daily interval, δ_V gradually became less negative as each campaign progressed, indicating the increasing contribution of heavier δ_T . An exception was noted on June 12—a lighter δ_V with a noticeable diurnal variation. This exception might have been due to a transition in the weather system caused by advection of a different air mass (Fig. 3, c and d).

4.3. Isotopic partitioning of ET

4.3.1. Determination of δ_{ET}

The effectiveness of Keeling-plot regression was low for both isotopes, especially for $\delta^{18}{\rm O}$ in Campaign 2. The coefficient of determination ($R_{keeling}^2$) between high-frequency δ_V and $1/\omega$ was 0.48 ± 0.30 for $\delta^2{\rm H}$ and 0.27 ± 0.22 for $\delta^{18}{\rm O}$ during Campaign 1, and was 0.35 ± 0.30 for $\delta^2{\rm H}$ and 0.08 ± 0.13 for $\delta^{18}{\rm O}$ during Campaign 2 (Fig. 7). The raw data of δ_V obtained from the WS-CRDS analyzer and the hourly regression results are illustrated in the Supplementary materials (Figs. S6 and S7). The lowest $R_{keeling}^2$ values were seen on June 27 (0.05 ± 0.07 for $\delta^2{\rm H}$ and 0.03 ± 0.03 for $\delta^{18}{\rm O}$). The average value of $R_{keeling}^2$ was significantly higher for $\delta^2{\rm H}$ than for $\delta^{18}{\rm O}$ during both campaigns (one-tailed paired-sample t-test, p-value < 0.001). The percentage of significant regression (p-value from the F test ≤ 0.05) was usually high (> 80%), except for $\delta^{18}{\rm O}$ in Campaign 2 (56.7%).

The effectiveness of Keeling-plot regression for $\delta^2 H$ was more explainable than for $\delta^{18} O$ by variations in both δ_V and ω . Based on Spearman's rank correlation analysis, the correlation between $R^2_{keeling_^2 H}$ and the standard deviation (SD) of $\delta_{V_^2 H}$ was strongly positive (R = 0.73, p-value ≤ 0.001), and the correlation between $R^2_{keeling_^2 H}$ and the SD of ω was moderately positive (R = 0.56, p-value ≤ 0.001). In contrast, the correlation between $R^2_{keeling_^{18} O}$ and the SD of $\delta_{V_^{18} O}$ was only weakly positive (R = 0.27, p-value ≤ 0.05) and that between $R^2_{keeling_^{18} O}$ and ω was strongly negative (R = -0.62, p-value ≤ 0.001).

We filtered hourly δ_{ET} solely based on δ^2 H (p-value threshold from the F test ≤ 0.05 and $R_{keeling_^2H}^2 > 0.40$), and we removed suspicious outliers showing unusually high δ_{ET} values (n = 4). After filtering, 57.1%

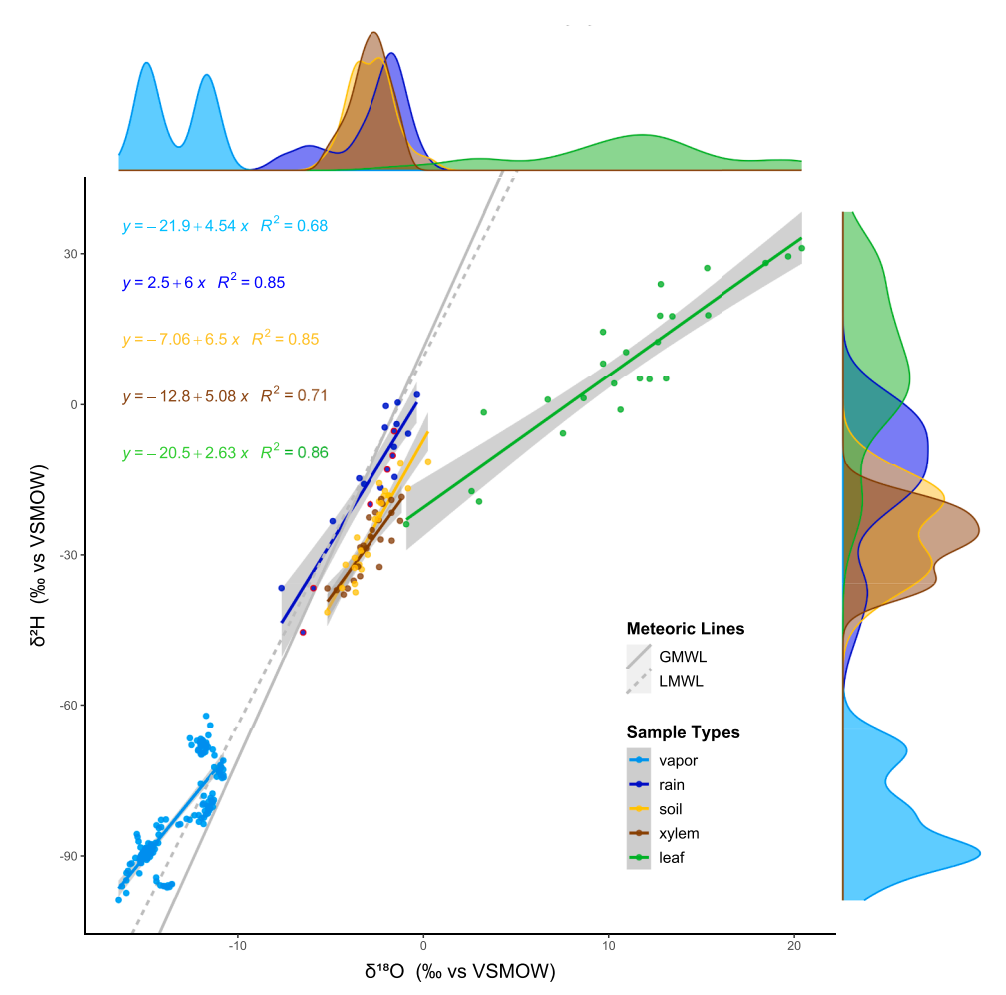


Fig. 5. Dual-isotope plot of water from various ecohydrological pools (upper 15-cm soil layer, plant leaves, root xylem, and near-ground atmospheric vapor during the two campaigns; and rainfall throughout 2016). The plot also includes two meteoric lines: the gray dots represent the Local Meteoric Water Line (LMWL, $\delta^2 H = 7.32 \ \delta^{18} O + 9.5$), from a long-term observation in Norman, OK (Jaeschke et al., 2011); and the solid gray line represents the Global Meteoric Water Line (GMWL, $\delta^2 H = 8.20 \ \delta^{18} O + 11.3$) (Rozanski et al., 2013).

and 46.7% of raw δ_{ET} data were retained for Campaigns 1 and 2, respectively. Note that this filtering removed all raw δ_{ET} data for June 27, when weather conditions were static, cloudy, and humid; thus, no data for that date were included in the ET partitioning analysis. The mean values of filtered hourly δ_{ET} across the two campaigns were -42.3 \pm 13.1 % for δ^2 H and -8.11 \pm 3.00 % for δ^{18} O (Fig. 8 and Table 1). The standard errors inherited from the linear regression were 1.72 \pm 0.84 % and 0.66 \pm 0.39 % for δ^2 H and δ^{18} O, respectively.

4.3.2. Determination of δ_E and δ_T

The proportions of the two fractionation factors (ε_{eq} vs ε_k) in the Craig–Gordon model (Eq. 3) were different for the two isotopes (Fig. 9). For δ^2 H, the values of ε_{eq} and ε_k differed by nearly one order of magnitude, whereas for δ^{18} O they were comparable and thus closely approached the 1:1 line. Diurnal patterns were characterized by higher ε_{eq} in the morning due to low soil temperature (Eq. 4a and 4b), and by higher ε_k (especially for δ^{18} O) during noontime and afternoon due to low relative humidity (and high *VPD*). The mean values of δ_E across the two field campaigns were -157 \pm 49.6 % for δ^2 H, and -30.9 \pm 4.15 % for δ^{18} O (Fig. 8 and Table 1). The errors in δ_E —propagated only from analysis uncertainty—were 0.82 \pm 0.45 % for δ^2 H and 0.16 \pm 0.08 % for δ^{18} O.

The daily δ_T values derived from δ_X based on the ISS assumption were relatively stable during the two campaigns (Fig. 8 and Table 1). The mean values of δ_T were -27.1 \pm 6.23 % for δ^2 H and -2.79 \pm 0.82 % for δ^{18} O. The errors in δ_T , propagated only from analysis uncertainty, were 0.89 \pm 0.27 % for δ^2 H and 0.11 \pm 0.08 % for δ^{18} O. We

acknowledge that errors in δ_E and δ_T are likely underestimated in our study due to no replicates in field sampling and dynamic variations in the evaporation front across the profile.

4.3.3. Dealing with uncertainties involved in isotopic ET partitioning

As expected from the two-source mixing model (Eq. 1), δ_{ET} largely varied between the isotopically light δ_E and the heavier δ_T at diurnal (Fig. 8) and daily scales (Table 1). Over the course of each campaign, daily δ_{ET} values gradually approached those of δ_T while progressively deviating from δ_E —indicating the increasing dominance of plant transpiration.

For partitioning of ET at the daily interval, we used $\delta^2 H$ rather than $\delta^{18} O$. We obtained a mean daily T/ET value (range) of 0.84 ± 0.05 (from 0.66 to 0.99) during Campaign 1, and of 0.92 ± 0.06 (from 0.86 to 0.98) during Campaign 2. The associated uncertainty levels were 0.12 ± 0.02 and 0.10 ± 0.02 for Campaigns 1 and 2, respectively (Fig. 10). The fact that the mean error value for daily δ_{ET} was 1.12 ± 0.69 —vs. 0.07 ± 0.07 , and 0.77 ± 0.22 , for δ_E and δ_T , respectively—shows that the error in daily δ_{ET} is the major source of uncertainty in T/ET results.

The actual fluxes of E and T exhibited greater variations in Campaign 1 than in Campaign 2 (Fig. 11). During Campaign 1, mean daily ET was 4.62 ± 0.04 mm day $^{-1}$, vs. 3.98 ± 0.07 mm day $^{-1}$ during Campaign 2. Within nine days following the precipitation event of June 3, daily T increased to above 4 mm day $^{-1}$, and by the end of Campaign 1 daily E had dropped below 0.20 mm day $^{-1}$. Following the relatively small rainfall events just before Campaign 2, the daily T fell below 4 mm day $^{-1}$ and decreased steadily, while the daily E flux dropped to a negligible level at the end of Campaign 2. The uncertainty level was the same for

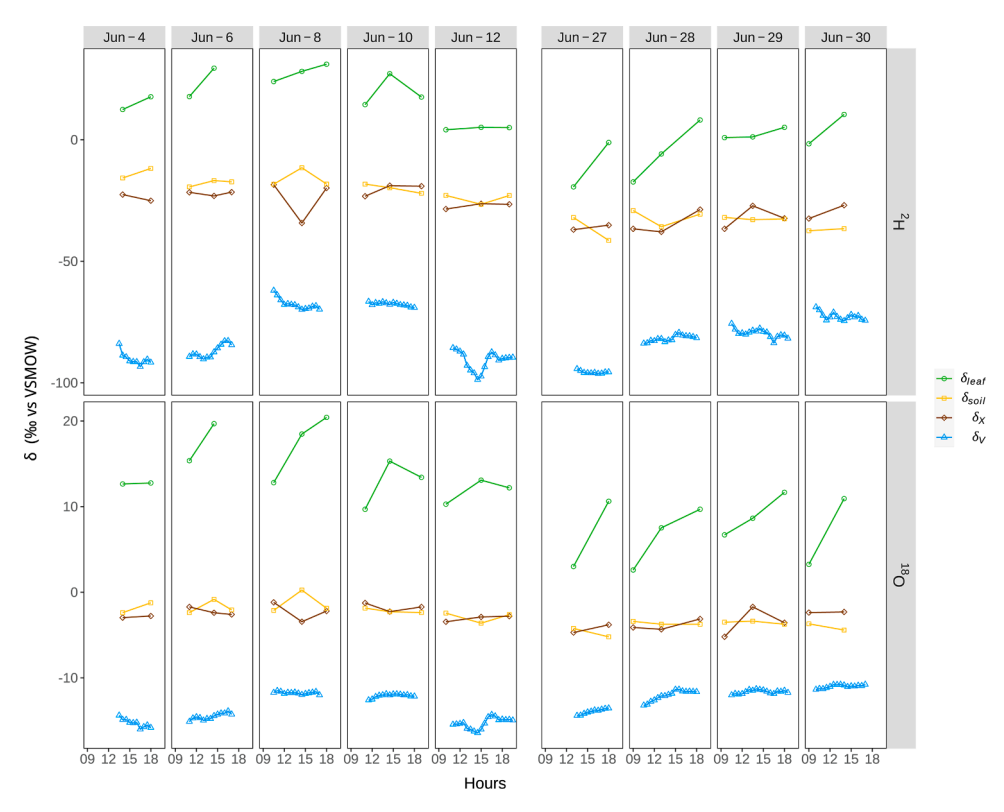
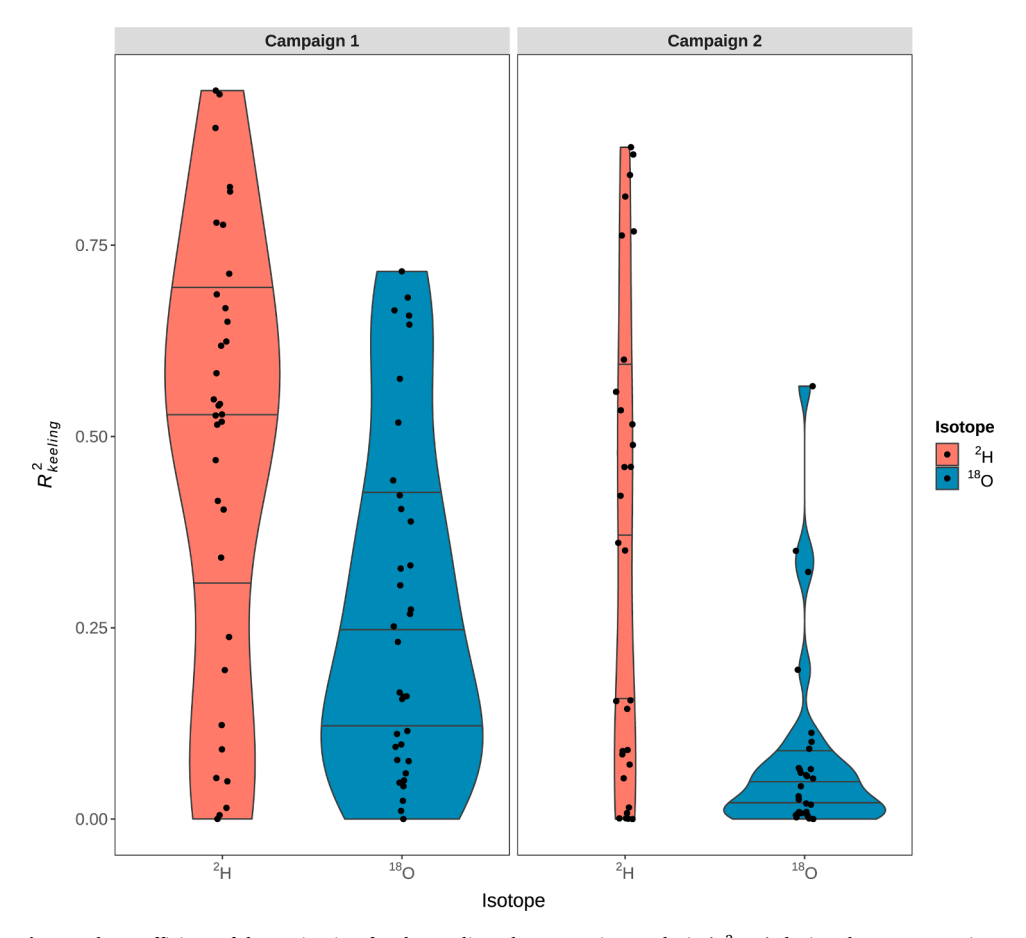


Fig. 6. Time series of the isotopic composition of sampled water in various ecohydrological pools during the two field campaigns. These pools include atmospheric water vapor (δ_V) measured at the three heights, liquid water in the surface soil layer (δ_{soil}) , plant xylem water (δ_X) , and bulk leaf water (δ_{leaf}) .



 $\textbf{Fig. 7.} \ \ \textbf{The coefficient of determination for the Keeling-plot regression analysis } (R^2_{\textit{keeling}}) \ \ \text{during the two campaigns}.$

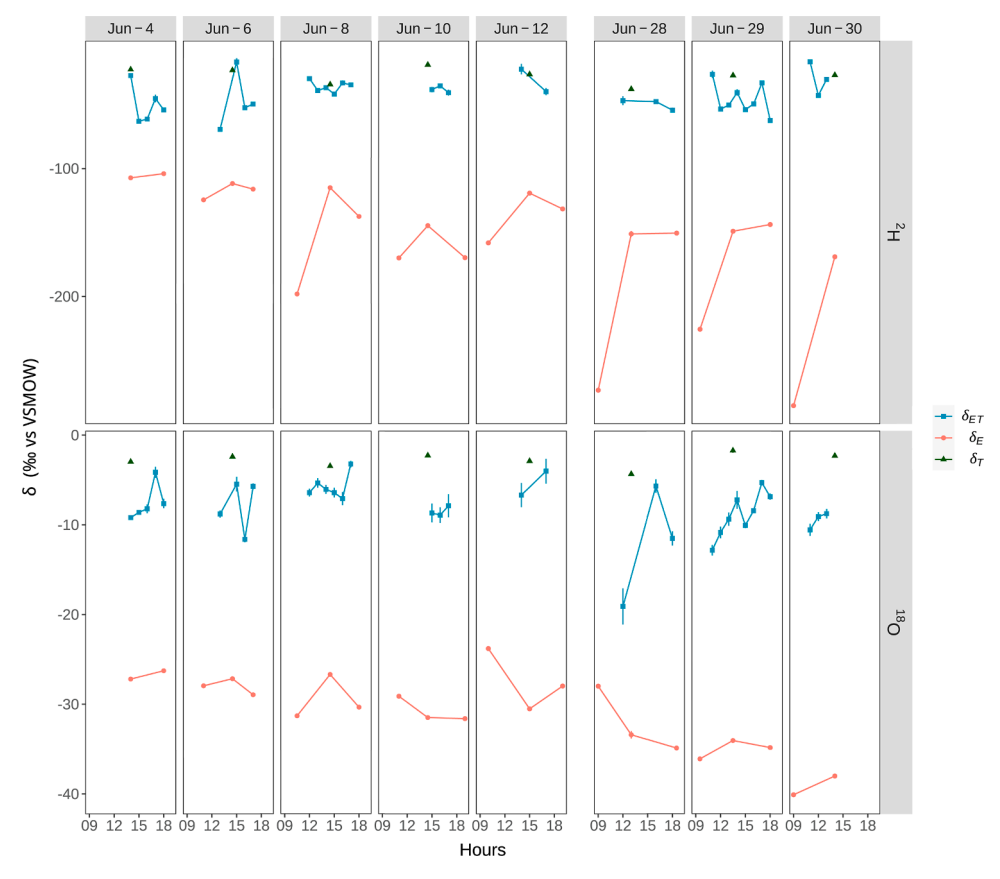


Fig. 8. Diurnal and daily dynamics of δ_{ET} , δ_{E} , and δ_{T} during the two field campaigns. Each error bar represents the standard deviation for its associated value.

Table 1 Mean \pm standard deviation for daily δ_{ET} , δ_{E} , and δ_{T} during the two campaigns.

Campaign	Date	² H			¹⁸ O		
		δ_{ET}	δ_E	δ_T	δ_{ET}	δ_E	δ_T
1	June 4	-50.6 ± 0.76	-106 ± 0.61	-22.6 ± 0.72	-7.65 ± 0.19	-26.7 ± 0.07	-2.97 ± 0.14
	June 6	$\textbf{-48.6} \pm \textbf{0.85}$	$\textbf{-117} \pm \textbf{0.57}$	$\textbf{-23.1} \pm \textbf{1.41}$	$\textbf{-8.26} \pm \textbf{0.24}$	$\textbf{-28.0} \pm 0.06$	-2.40 ± 0.04
	June 8	$\textbf{-35.7} \pm 0.58$	$\textbf{-144} \pm 0.34$	$\textbf{-34.2} \pm 1.10$	$\textbf{-5.80} \pm 0.22$	-29.1 ± 0.07	$\textbf{-3.45} \pm 0.08$
	June 10	-37.9 ± 1.14	$\textbf{-160} \pm \textbf{0.26}$	$\textbf{-}18.9 \pm 0.54$	$\textbf{-8.54} \pm \textbf{0.61}$	$\textbf{-30.8} \pm 0.11$	-2.27 ± 0.03
	June 12	$\textbf{-30.2} \pm \textbf{2.56}$	$\textbf{-135} \pm \textbf{0.59}$	$\textbf{-26.3}\pm\textbf{0.77}$	$\textbf{-5.48} \pm \textbf{0.97}$	$\textbf{-27.8} \pm 0.11$	$\textbf{-2.89} \pm 0.08$
2	June 28	-48.3 ± 1.69	-176 \pm 1.13	-37.9 ± 0.83	-12.4 ± 0.94	-32.8 ± 0.20	-4.34 ± 0.07
	June 29	$\textbf{-45.8} \pm 0.64$	$\textbf{-160} \pm \textbf{0.43}$	$\textbf{-27.2} \pm 0.94$	$\textbf{-8.95} \pm \textbf{0.22}$	$\textbf{-34.8} \pm 0.09$	$\textbf{-1.72} \pm \textbf{0.25}$
	June 30	-30.9 ± 0.74	$\textbf{-207} \pm \textbf{0.83}$	-26.9 ± 0.82	-9.45 ± 0.33	$\textbf{-38.7} \pm 0.17$	-2.31 ± 0.20

Values are expressed as mean \pm one standard deviation.

The uncertainty level for δ_{ET} was derived from the standard error of the OLS regression, and uncertainties in δ_{E} and δ_{T} were propagated mainly from the analysis error.

daily *E* and *T* fluxes, and was 0.49 ± 0.13 mm day⁻¹ on average.

4.4. Response of ET partitioning during two drying-up episodes

The variability in daily T/ET was initially driven by an intense drying process of shallow soil water shortly after precipitation, and thereafter was more controlled by micro-meteorological processes. Isotopic analysis based on δ^2 H showed a dramatic increase in daily T/ET during Campaign 1—from 0.66 ± 0.11 to 0.99 ± 0.11 —within five days following precipitation events (Fig. 10). We were unable to observe a similar pattern in daily T/ET during the early part of Campaign 2, because δ_{ET} was unavailable (owing to the low effectiveness of Keeling-plot regression for June 27). Once the shallow soil moisture had dried up, atmospheric processes became stronger influences on day-to-day variations in T/ET. For example, daily T/ET decreased on both June 10 and June 29, coincident with the highest T_{air} level for Campaign 1

and the highest VPD level for Campaign 2, respectively.

As shown in Fig. 11, the distinct temporal patterns of soil evaporation and plant transpiration caused variations in reduction of soil water storage throughout the profile. At the beginning of each campaign, soil water availability in the shallow layers was moderately high but decreased quickly as a result of the high *E* flux, especially for the top 10-cm layer (Fig. 4). This surface layer was the dominant source of *E* during the first half of Campaign 1 and most of Campaign 2. Then, as $\Delta\theta_{soil}$ for the top 10-cm layer gradually decreased and daily *E* dropped, *T* gradually increased, fed by soil moisture from the deeper layers. In particular, the reduction of θ_{soil} from the bottom layer (60–100 cm) was small and intermittent during Campaign 1 but became a major factor by the end of Campaign 2. This trend of reduction of moisture from the deeper levels from one campaign to the next accounted for a divergence in the pattern of soil moisture profiles between the two campaigns (Fig. 4).

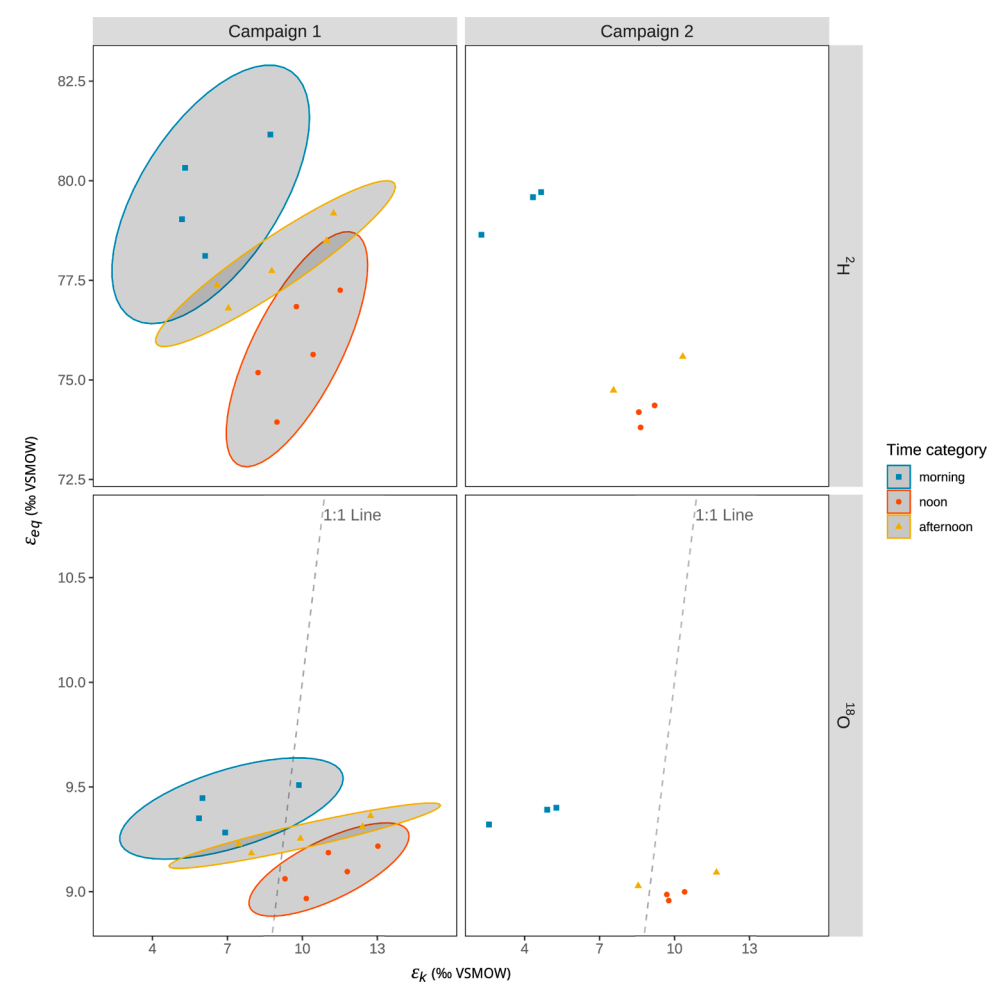


Fig. 9. Equilibrium fractionation factor ε_{eq} (‰) versus kinetic fractionation factor ε_k (‰) for δ^2 H and δ^{18} O. The confidence level for the ellipses is 0.8. Data for June 27 were not included. Because of the small data size, ellipses were not drawn for Campaign 2.

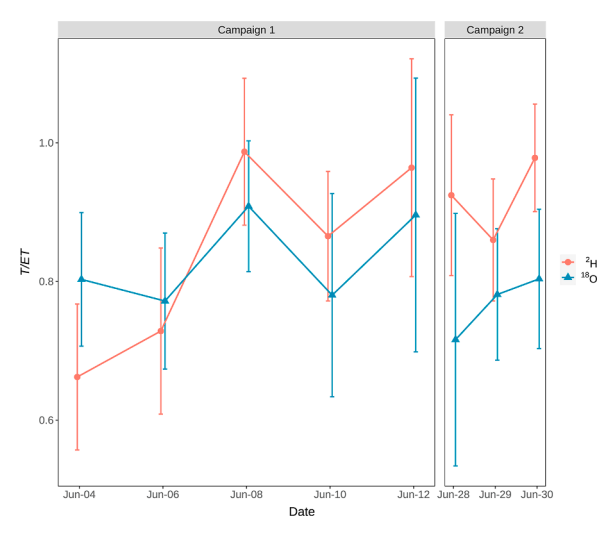


Fig. 10. Temporal variations in T/ET at the daily interval. Each error bar represents the daily standard deviation of T/ET for each sampling day.

5. Discussion

5.1. Analysis of uncertainties in the isotopic two-source mixing model

Accurate partitioning of ET depends on clearly distinguishing

between the values $\overline{\delta_E}$ and $\overline{\delta_T}$ on the one hand, and accurately quantifying δ_{ET} , δ_E , and δ_T on the other hand (Eq. 8). Because the partitioning result is especially sensitive to δ_{ET} , accurate quantification of this variable is important—but remains a key challenge (Good et al., 2014; Hu et al., 2014; Marshall et al., 2007; Sutanto et al., 2014; Wang and Yakir, 2000).

The level of error in estimation of δ_{ET} is the biggest source of uncertainty in our study. The Keeling-plot method optimally applies to sites characterized by substantial temporal variations in δ_V brought about exclusively by a strong ET flux during a short period (Hu et al., 2014). But such conditions rarely exist in natural environments (Lee et al., 2006). The relatively low effectiveness shown in our Keeling-plot regression, especially for δ^{18} O, signified that the correlation between δ_V and the reciprocal of the molar mixing ratio of water vapor $(1/\omega)$ was relatively weak. A similar case was reported for a rice paddy field, where only 24% of the hourly $\delta_{ET_^2H}$ data met the filtering standards, namely, a sufficient sample size (N > 40) and a sufficiently high coefficient of determination ($R_{keeling}^2 > 0.8$) (Wei et al., 2015). One reason for the low regression effectiveness could be the existence of highly variable in situ micro-meteorological conditions; for example, advection (Lee et al., 2006) and entrainment (Lee et al., 2012) can be major causes of variations in δ_V at hourly to daily scales. Another reason for this low effectiveness might be that the δ_{ET} values are not clearly distinguishable from the isotopic composition of the background atmosphere (δ_{bg}), resulting in a less noticeable gradient in δ_V among the three measurement heights (Fig. 6). Because June 27 was characterized by cloudy, stagnant, humid weather and a decreased ET, such a small vertical gradient in δ_V could

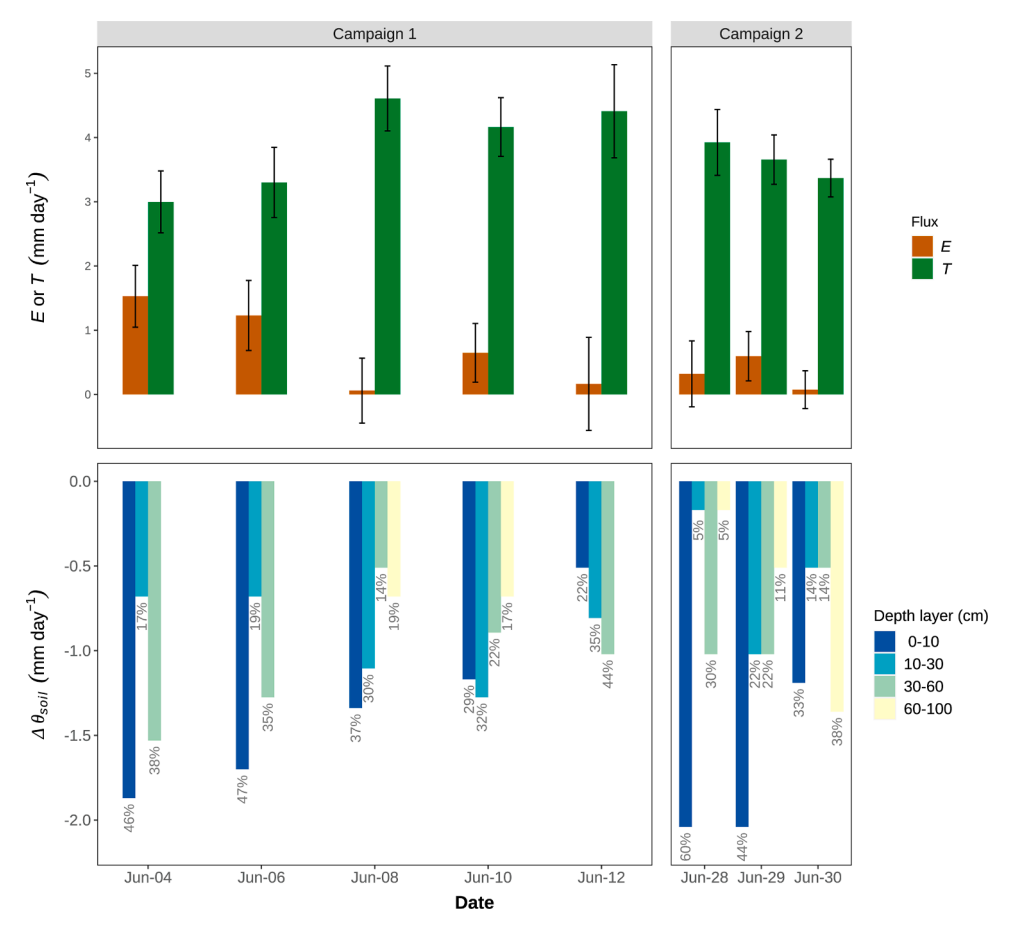


Fig. 11. Variations in daily fluxes of *E* and *T* as shown by partitioning based on δ^2 H, and associated variations in volumetric soil water content ($\Delta\theta_{soil}$) at different depths. Error bars for *E* and *T* represent one standard deviation. Percentages shown for the $\Delta\theta_{soil}$ bars represent the water storage change of each layer as a percentage of the total soil column. Note that the $\Delta\theta_{soil}$ bar for June 30 is derived only from measurements prior to a precipitation event at 17:00 that day.

appear essentially negligible; thus, no satisfactory δ_{ET} results were obtained for that day.

In parallel to the uncertainties in estimating δ_{ET} , there are uncertainties involved in the quantification of δ_E and δ_T . For the Craig–Gordon model (Eq. 3), identification of the evaporation front is essential for accurate measurement of δ_{Se} , T_{soil} , and h (Dubbert et al., 2013; Xiao et al., 2018). Substituting δ_{soil} of the bulk surface soil layer for δ_{Se} could introduce large uncertainties into the estimation of δ_E , owing to the high temporal and spatial variability in the isotopic composition of soil water (Oerter and Bowen, 2019; Sprenger et al., 2017). For example, in a tallgrass prairie pasture, noticeable variations in δ_{soil} were observed in the top 20 cm of soil (Riley et al., 2003).

The use of laser spectroscopy for direct, continuous, and non-destructive sampling of pore water (liquid or vapor) in the vadose zone (Gaj et al., 2016; Oerter et al., 2017; Rothfuss et al., 2013; Sprenger et al., 2015; Volkmann and Weiler, 2014) is a promising technique for locating the evaporation front (Soderberg et al., 2012) or for direct quantification of δ_E with high temporal and spatial resolution. Although plant transpiration may violate the ISS assumption in mornings and evenings (Farquhar and Cernusak, 2005; Welp et al., 2008; Yepez et al., 2005), assuming ISS conditions are met during the midday hours, deriving δ_T directly from measured δ_X is a widely adopted practice (Wen et al., 2016; Williams et al., 2004; Yepez et al., 2003; Zhang et al., 2018).

5.2. Selection of an isotope for T/ET analysis ($\delta^2 \mathbf{H}$ vs $\delta^{18} \mathbf{O}$)

We selected $\delta^2 H$ for T/ET partitioning because of its higher effectiveness in Keeling-plot regressions of high-temporal-resolution δ_V data

and its greater values of equilibrium fractionation involved in evaporation. The higher effectiveness we found for $\delta^2 H$ vs. $\delta^{18} O$ in Keeling-plot regressions is consistent with the findings of previous, related investigations (Aouade et al., 2016; Xu et al., 2008). One reason might be that greater variability in the hydrogen-related isotopologues was responsible for the more significant and stronger relationship between $R_{keeling}^2$ and variations in $\delta_{V_-^2H}$. The poorer effectiveness of δ^{18} O in Keeling-plot regressions was particularly evident during Campaign 2, when conditions were more humid and $R_{keeling}^2$ was observed to be inversely proportional to ω (possibly because $\varepsilon_{k_-^{18}O}$ declines under high humidity, resulting in smaller gradients in $\delta_{V_{-}^{18}O}$ during vapor diffusion). In other words, the robustness of the Keeling-plot regression based on $\delta^{18}\mathrm{O}$ is jeopardized under humid conditions. The second reason for the higher effectiveness of δ^2 H might be its lower error level with respect to dependence on water vapor concentrations for the WS-CRDS analyzer, especially when ω is either extremely low or extremely high (Sprenger et al., 2015; Wen et al., 2012). The third reason for choosing δ^2 H was related to the different sensitivities of δ^2 H and δ^{18} O to equilibrium and kinetic fractionation processes (Risi et al., 2010): the value of ε_{eq} was dramatically higher for $\delta^2 H$ than for $\delta^{18} O$ —thus, $\delta^2 H$ could yield a lower δ_E and a pronounced distinction between $\overline{\delta_E}$ and $\overline{\delta_T}$. This pronounced distinction could greatly constrain the uncertainties involved in T/ET analysis (Eq. 8). For example, the uncertainty levels for δ^2 H and δ^{18} O in our T/ET results were comparable even though the errors involved in δ_{ET} , δ_{E} , and δ_{T} were higher for δ^{2} H than for δ^{18} O.

5.3. Pattern of ET partitioning during wetting-drying episodes

A decrease–increase in the T/ET pattern is often observed during the wetting-drying episodes associated with water inputs. For example, a study in an olive plantation revealed that T/ET was 100% during the preceding dry periods but dropped to 0.69–0.85 at midday following precipitation events (Williams et al., 2004). Another study, of a semiarid winter wheat cropland, found that average T/ET was 0.80 when the soils were dry and dropped to 0.69 three days after precipitation (Aouade et al., 2016). This transient effect of rainfall events on ET partitioning—i.e., suppression of T and enhancement of E—were also observed in a cornfield in the immediate aftermath of rainfall events (up to several days) (Scanlon and Kustas, 2010). During Campaign 1 of our study, the transient decrease in T/ET was followed by an increase, from 0.66 to 0.99, during the five-day drying periods. A similar trend was also observed in a semiarid grassland in southeastern Arizona, USA, where mean daily T/ET increased during three days of drying following a 39-mm irrigation event, from 0.35 to 0.43 (Yepez et al., 2005). Overall short-term T/ET results for our study (which ranged from 0.84 to 0.92 for our two campaigns) were consistent with those of other pertinent studies. For example, a six-day study in a temperate grassland reported an average T /ET of 0.83 (Hu et al., 2014). In grassland ecosystems having a dense canopy, daily T/ET can increase to a maximum value of 0.9 ($LAI > 3 \text{ m}^2 \text{ m}^{-2}$) (Hu et al., 2009).

5.4. Soil water availability and root water uptake

In the mesic tallgrass prairie, most of the soil evaporation comes from water storage in shallow (10–20 cm depth) soils (Marshall et al., 2007), while the roots of the majority of C₄ grasses—which are highly functional in water uptake and leaf transpiration—are distributed throughout the 1-m depth (Nippert et al., 2012). Though our mere observation of changes in water storage across the profile could not discriminate between water losses from *E* and those from *T*, the similarities in isotopic composition of plant xylem water and soil water in the 15-cm-depth layer, as well as the great variability in shallow soil water storage, are evidence that the shallow soil layers (especially the top 10 cm, until depletion) were the major sources for both *E* and *T*. As shallow soil moisture became depleted, root uptake gradually shifted to deeper soil layers (as deep as 1 m) to supply plant transpiration. A study in an irrigated winter wheat cropland found a similar deepening trend in root water uptake (Yang et al., 2018).

The mechanisms involved in root water uptake reflect the plant's survival strategy (Wang et al., 2018). Because of methodological limitations, our study was not able to fully describe the dynamics and mechanisms of root water uptake across the profile in response to changes in water availability-which would require high-resolution probing of stable water isotopes in soil and transpiration water using laser spectroscopy (Sprenger et al., 2015; Volkmann et al., 2016). Our short-term results were able to identify a certain flexibility in root water uptake; but given that the timescales at which vegetation is observationally affected by drought in semiarid and subhumid biomes are relatively long (Vicente-Serrano et al., 2013), longer-term investigations of ET partitioning and vegetation responses will be needed to assess the sustainability of the tallgrass prairie under climate change—especially with the predicted decreases in soil water availability (Knapp et al., 2002; Sala et al., 2015) due to precipitation changes and drier summers (Raz-Yaseef et al., 2015).

6. Conclusions

Evapotranspiration involves complex biophysical mechanisms that drive energy and mass exchanges between the land surface and atmosphere. The partitioning of ET is critical for elucidating these complex mechanisms, and it is also essential for assessing plant water use efficiency, which enables monitoring of ecosystem functioning and of ecosystem hydrologic response to climate change and land cover change. We carried out an isotopic ET partitioning study on a mesic

grassland in tallgrass prairie, during two dynamic wetting–drying episodes. We employed an isotopic two-source mixing model, for which (1) δ_{ET} was obtained by applying the Keeling-plot regression to high-frequency isotopic measurements of water vapor acquired by a field-deployable laser spectrometer; (2) δ_E was calculated by applying the Craig–Gordon model; and (3) δ_T was estimated under the isotopic steady-state assumption.

We found the effectiveness of the Keeling-plot regressions to be low, but this low effectiveness was explainable (more so for δ^2H than for δ^{18} O) by variations in both the molar mixing ratio and the isotopic composition of atmospheric water vapor. For δ_E , the equilibrium fractionation process was dramatically stronger for δ^2H than for $\delta^{18}O$, resulting in greater differences between mean values of δ_E and δ_T . For these reasons, we selected $\delta^2 H$ for the two-source mixing model. During Campaign 1, we observed a dramatic increase in daily T/ET (from 0.66 to 0.99) within five days of drying following precipitation, but a similar pattern was not observed during Campaign 2-probably because the initial quantification of δ_{ET} was poor. The mean values of daily T/ETwere 0.84 \pm 0.05 and 0.92 \pm 0.06 for Campaigns 1 and 2, respectively. The difference is possibly attributable to the dissimilar soil water availability across the profile. Although our two short field campaigns in tallgrass prairie provide insights into the dynamics of ET partitioning following precipitation, as well as root water uptake within the 1-m depth, a more in-depth understanding of the interplay between soil water availability and ET partitioning will require further investigations. Longer-term studies—including isotopic sampling of soil water vapor and plant water with high temporal resolution—are needed to serve as a foundation for sustainable management of the endangered tallgrass prairie and its ecosystem services under current and predicted environmental conditions.

Declaration of Competing Interest

The authors declare that they have no known competing financial interests or personal relationships that could have appeared to influence the work reported in this paper.

Acknowledgements

This work is funded by the Dynamics of Coupled Natural and Human Systems (CNH) program of the National Science Foundation (contract number: DEB-1413900). We are grateful to Chris Stansberry for maintaining the study site. We appreciated field assistance by Patricia Torquato and Giovanne Serrau from Oklahoma State University. We also express our appreciation to Dr. Donald L. Phillips from the U.S. Environmental Protection Agency for his assistance in the uncertainty analysis. We greatly appreciate the anonymous reviewers for their insightful and constructive comments.

Supplementary materials

Supplementary material associated with this article can be found, in the online version, at doi:10.1016/j.agrformet.2021.108321.

References

Adams, Rachel E., Hyodo, Ayumi, SantaMaria, Toby, Wright, Cynthia L., Boutton, Thomas W., West, Jason B., 2020. Bound and mobile soil water isotope ratios are affected by soil texture and mineralogy, whereas extraction method influences their measurement. Hydrol. Proc. 34 (4), 991–1003. https://doi.org/ 10.1002/hyp.13633.

Aouade, G., Ezzahar, J., Amenzou, N., Er-Raki, S., Benkaddour, A., Khabba, S., Jarlan, L., 2016. Combining stable isotopes, Eddy Covariance system and meteorological measurements for partitioning evapotranspiration, of winter wheat, into soil evaporation and plant transpiration in a semi-arid region. Agric. Water Manag. 177, 181–192. https://doi.org/10.1016/j.agwat.2016.07.021.

Archer, Steven R., Andersen, Erik M., Predick, Katharine I., Schwinning, Susanne, Steidl, Robert J., Woods, Steven R., 2017. Woody Plant Encroachment: Causes and

- Consequences. In: Briske, David D. (Ed.), Rangeland Systems: Processes, Management and Challenges. Springer International Publishing, Cham, pp. 25–84. https://doi.org/10.1007/978-3-319-46709-2 2.
- Bachmann, D., Gockele, A., Ravenek, J.M., Roscher, C., Strecker, T., Weigelt, A., Buchmann, N., 2015. No Evidence of Complementary Water Use along a Plant Species Richness Gradient in Temperate Experimental Grasslands. PLoS One 10 (1). https://doi.org/10.1371/journal.pone.0116367.
- Barnard, R.L., de Bello, F., Gilgen, A.K., Buchmann, N., 2006. The δ^{18} O of root crown water best reflects source water δ^{18} O in different types of herbaceous species. Rapid Commun. Mass Sp. 20 (24), 3799–3802. https://doi.org/10.1002/rcm.2778.
- Berkelhammer, M., Noone, D.C., Wong, T.E., Burns, S.P., Knowles, J.F., Kaushik, A., Blanken, P.D., Williams, M.W., 2016. Convergent approaches to determine an ecosystem's transpiration fraction. Global Biogeochem. Cy. 30 (6), 933–951. https://doi.org/10.1002/2016GB005392.
- Blyth, E., Harding, R.J., 2011. Methods to separate observed global evapotranspiration into the interception, transpiration and soil surface evaporation components. Hydrol. Proc. 25 (26), 4063–4068. https://doi.org/10.1002/hyp.8409.
- Bowen, G.J., Cai, Z., Fiorella, R.P., Putman, A.L., 2019. Isotopes in the Water Cycle: Regional- to Global-Scale Patterns and Applications. Annu. Rev. Earth Planet. Sci. 47 (1), 453–479. https://doi.org/10.1146/annurev-earth-053018-060220.
- Braud, I., Bariac, T., Gaudet, J.P., Vauclin, M., 2005a. SiSPAT-Isotope, a coupled heat, water and stable isotope (HDO and H₂¹⁸O) transport model for bare soil. Part I. Model description and first verifications. J. Hydrol. 309 (1-4), 277–300. https://doi.org/10.1016/j.jhydrol.2004.12.013.
- Braud, I., Bariac, T., Vauclin, M., Boujamlaoui, Z., Gaudet, J.P., Biron, Ph., Richard, P., 2005b. SiSPAT-Isotope, a coupled heat, water and stable isotope (HDO and H₂⁸O) transport model for bare soil. Part II. Evaluation and sensitivity tests using two laboratory data sets. J. Hydrol. 309 (1-4), 301–320. https://doi.org/10.1016/j.ibydrol.2004.12.012
- Brooks, J.R., 2015. Water, bound and mobile. Science 349 (6244), 138–139. https://doi.org/10.1126/science.aac4742.
- Brunel, J.P., Walker, G.R., Dighton, J.C., Monteny, B., 1997. Use of stable isotopes of water to determine the origin of water used by the vegetation and to partition evapotranspiration. A case study from HAPEX-Sahel. J. Hydrol. 188–189 (1-4), 466–481. https://doi.org/10.1016/S0022-1694(96)03188-5.
- Buck, A.L., 1981. New Equations for Computing Vapor-Pressure and Enhancement Factor. J. Appl. Meteorol. 20 (12), 1527–1532. https://doi.org/10.1175/1520-0450 (1981)020<1527:NEFCVP>2.0.CO:2.
- Cappa, C.D., Hendricks, M.B., DePaolo, D.J., Cohen, R.C., 2003. Isotopic fractionation of water during evaporation. J. Geophys. Res. Atmos. 108 (D16), 4525. https://doi. org/10.1029/2003JD003597.
- Chapman, K., White, M., Johnson, R., Wong, Z., 1990. An approach to evaluate long-term survival of the tallgrass prairie ecosystem. The Nature Conservancy. Midwest Regional Office, Minneapolis, MN, p. 50.
- Craig, H., 1961. Isotopic Variations in Meteoric Waters. Science 133 (3465), 1702–1703. https://doi.org/10.1126/science.133.3465.1702.
- Craig, H., Gordon, L.I., 1965. Deuterium and oxygen 18 variations in the ocean and the marine atmosphere. Stable Isotopes in Oceanographic Studies and Paleotemperatures. Consiglio nazionale delle richerche, Laboratorio de geologia nucleare, Pisa, Spoleto, Italy, pp. 9–130.
- Dubbert, M., Cuntz, M., Piayda, A., Maguas, C., Werner, C., 2013. Partitioning evapotranspiration - Testing the Craig and Gordon model with field measurements of oxygen isotope ratios of evaporative fluxes. J. Hydrol. 496, 142–153. https://doi. org/10.1016/j.jhydrol.2013.05.033.
- Dubbert, M., Piayda, A., Cuntz, M., Correia, A.C., Costa e Silva, F., Pereira, J.S., Werner, C., 2014. Stable oxygen isotope and flux partitioning demonstrates understory of an oak savanna contributes up to half of ecosystem carbon and water exchange. Front. Plant Sci. 5. 530. https://doi.org/10.3389/fpis.2014.00530.
- Durand, J.L., Bariac, T., Ghesquière, M., Biron, P., Richard, P., Humphreys, M., Zwierzykovski, Z., 2007. Ranking of the depth of water extraction by individual grass plants, using natural ¹⁸O isotope abundance. Environ. Exp. Bot. 60 (1), 137–144. https://doi.org/10.1016/j.envexpbot.2006.09.004.
- Eggemeyer, K.D., Awada, T., Harvey, F.E., Wedin, D.A., Zhou, X., Zanner, C.W., 2009. Seasonal changes in depth of water uptake for encroaching trees Juniperus virginiana and Pinus ponderosa and two dominant C₄ grasses in a semiarid grassland. Tree Physiol. 29 (2), 157–169. https://doi.org/10.1093/treephys/tpn019.
- Ehleringer, J.R., Dawson, T.E., 1992. Water uptake by plants: perspectives from stable isotope composition. Plant Cell Environ. 15 (9), 1073–1082. https://doi.org/10.1111/j.1365-3040.1992.tb01657.x.
- Ehleringer, J.R., Roden, J., Dawson, T.E., 2000. Assessing ecosystem-level water relations through stable isotope ratio analyses. Methods in ecosystem science. Springer, New York, NY, pp. 181–198. https://doi.org/10.1007/978-1-4612-1224-9 13.
- Farquhar, G.D., Cernusak, L.A., 2005. On the isotopic composition of leaf water in the non-steady state. Functional Plant Biol. 32 (4), 293–303. https://doi.org/10.1071/ INDASO.
- Fatichi, S., Pappas, C., 2017. Constrained variability of modeled T:ET ratio across biomes. Geophys. Res. Lett. 44 (13), 6795–6803. https://doi.org/10.1002/ 2017GL074041.
- Fisher, J.B., Melton, F., Middleton, E., Hain, C., Anderson, M., Allen, R., McCabe, M.F., Hook, S., Baldocchi, D., Townsend, P.A., Kilic, A., Tu, K., Miralles, D.D., Perret, J., Lagouarde, J.P., Waliser, D., Purdy, A.J., French, A., Schimel, D., Famiglietti, J.S., Stephens, G., Wood, E.F., 2017. The future of evapotranspiration: Global requirements for ecosystem functioning, carbon and climate feedbacks, agricultural management, and water resources. Water Resour. Res. 53 (4), 2618–2626. https:// doi.org/10.1002/2016WR020175.

- Freese, C.H., Fuhlendorf, S.D., Kunkel, K., 2014. A management framework for the transition from livestock production toward biodiversity conservation on great plains rangelands. Ecol. Restor. 32 (4), 358–368. https://doi.org/10.3368/ er.32.4.358
- Gaj, M., Beyer, M., Koeniger, P., Wanke, H., Hamutoko, J., Himmelsbach, T., 2016. In situ unsaturated zone water stable isotope (²H and ¹⁸O) measurements in semi-arid environments: a soil water balance. Hydrol. Earth Syst. Sci. 20 (2), 715–731. https://doi.org/10.5194/hess-20-715-2016.
- Gat, J.R., 1996. Oxygen and hydrogen isotopes in the hydrologic cycle. Annu. Rev. Earth Planet. Sci. 24 (1), 225–262. https://doi.org/10.1146/annurev.earth.24.1.225.
- Good, S.P., Noone, D., Bowen, G., 2015. Hydrologic connectivity constrains partitioning of global terrestrial water fluxes. Science 349 (6244), 175–177. https://doi.org/ 10.1126/science.aaa5931.
- Good, S.P., Soderberg, K., Guan, K., King, E.G., Scanlon, T.M., Caylor, K.K., 2014. 6²H isotopic flux partitioning of evapotranspiration over a grass field following a water pulse and subsequent dry down. Water Resour. Res. 50 (2), 1410–1432. https://doi.org/10.1002/2013WR014333.
- Good, S.P., Soderberg, K., Wang, L.X., Caylor, K.K., 2012. Uncertainties in the assessment of the isotopic composition of surface fluxes: A direct comparison of techniques using laser-based water vapor isotope analyzers. J. Geophys. Res. Atmos. 117 (D15) https://doi.org/10.1029/2011.JD017168.
- Gu, C., Ma, J., Zhu, G., Yang, H., Zhang, K., Wang, Y., Gu, C., et al., 2018. Partitioning evapotranspiration using an optimized satellite-based ET model across biomes. Agric. For. Meteorol. 259, 355–363. https://doi.org/10.1016/j. agric.part. 2018.05.023
- Horita, J., Rozanski, K., Cohen, S., 2008. Isotope effects in the evaporation of water: a status report of the Craig-Gordon model. Isot. Environ. Health Stud. 44 (1), 23–49. https://doi.org/10.1080/10256010801887174.
- Hu, Z., Wen, X., Sun, X., Li, L., Yu, G., Lee, X., Li, S., 2014. Partitioning of evapotranspiration through oxygen isotopic measurements of water pools and fluxes in a temperate grassland. J. Geophys. Res-Biogeo. 119 (3), 358–372. https://doi.org/ 10.1002/2013JG002367.
- Hu, Z., Yu, G., Zhou, Y., Sun, X., Li, Y., Shi, P., Wang, Y., Song, X., Zheng, Z., Zhang, L., Li, S., 2009. Partitioning of evapotranspiration and its controls in four grassland ecosystems: Application of a two-source model. Agric. For. Meteorol. 149 (9), 1410–1420. https://doi.org/10.1016/j.agrformet.2009.03.014.
- Keeling, C.D., 1958. The concentration and isotopic abundances of atmospheric carbon dioxide in rural areas. Geochim. Cosmochim. Ac. 13 (4), 322–334. https://doi.org/ 10.1016/0016-7037(58)90033-4.
- Knapp, A.K., Beier, C., Briske, D.D., Classen, A.T., Luo, Y., Reichstein, M., Smith, M.D., Smith, S.D., Bell, J.E., Fay, P.A., Heisler, J.L., Leavitt, S.W., Sherry, R., Smith, B., Weng, E., 2008. Consequences of more extreme precipitation regimes for terrestrial ecosystems. Bioscience 58 (9), 811–821. https://doi.org/10.1641/B580908.
- Knapp, A.K., Fay, P.A., Blair, J.M., Collins, S.L., Smith, M.D., Carlisle, J.D., Harper, C.W., Danner, B.T., Lett, M.S., McCarron, J.K., 2002. Rainfall variability, carbon cycling, and plant species diversity in a mesic grassland. Science 298 (5601), 2202–2205. https://doi.org/10.1126/science.1076347.
- Kool, D., Agam, N., Lazarovitch, N., Heitman, J.L., Sauer, T.J., Ben-Gal, A., 2014. A review of approaches for evapotranspiration partitioning. Agric. For. Meteorol. 184, 56–70. https://doi.org/10.1016/j.agrformet.2013.09.003.
- Lai, C.T., Ehleringer, J.R., Bond, B.J., U, K.T.P., 2006. Contributions of evaporation, isotopic non-steady state transpiration and atmospheric mixing on the δ¹⁸O of water vapour in Pacific Northwest coniferous forests. Plant Cell Environ. 29 (1), 77–94. https://doi.org/10.1111/j.1365-3040.2005.01402.x.
- Lee, X., Huang, J., Patton, E.G., 2012. A large-eddy simulation study of water vapour and carbon dioxide isotopes in the atmospheric boundary layer. Boundary-Layer Meteorol. 145 (1), 229–248. https://doi.org/10.1007/s10546-011-9631-3.
- Meteorol. 145 (1), 229–248. https://doi.org/10.1007/s10546-011-9631-3. Lee, X., Smith, R., Williams, J., 2006. Water vapour ¹⁸O/¹⁶O isotope ratio in surface air in New England, USA. Tellus B 58 (4), 293–304. https://doi.org/10.1111/j.1600-0889.2006.00101.x
- Li, X., Gentine, P., Lin, C., Zhou, S., Sun, Z., Zheng, Y., Liu, J., Zheng, C., 2019. A simple and objective method to partition evapotranspiration into transpiration and evaporation at eddy-covariance sites. Agric. For. Meteorol. 265, 171–182. https:// doi.org/10.1016/j.agrformet.2018.11.017.
- Limb, R.F., Engle, D.M., Alford, A.L., Hellgren, E.C., 2010. Tallgrass prairie plant community dynamics along a canopy cover gradient of eastern redcedar (Juniperus virginiana L.). Rangeland Ecol. Manage. 63 (6), 638–644. https://doi.org/10.2111/ REM-D-09-00056.1.
- Majoube, M., 1971. Fractionnement en oxygène 18 et en deutérium entre l'eau et sa vapeur. J. Chim. Phys. 68 (10), 1423–1436. https://doi.org/10.1051/jcp/1971681423. +.
- Marshall, J.D., Brooks, J.R., Lajtha, K., 2007. Sources of variation in the stable isotopic composition of plants. Stable Isotopes Ecol. Environ. Sci. 22–60. https://doi.org/ 10.1002/9780470691854.ch2.
- Mathieu, R., Bariac, T., 1996. An Isotopic Study (²H and ¹⁸O) of Water Movements in Clayey Soils Under a Semiarid Climate. Water Resour. Res. 32 (4), 779–789. https://doi.org/10.1029/96WR00074.
- McKinley, D.C., Blair, J.M., 2008. Woody plant encroachment by Juniperus virginiana in a mesic native grassland promotes rapid carbon and nitrogen accrual. Ecosystems 11 (3), 454–468. https://doi.org/10.1007/s10021-008-9133-4.
- Merlivat, L., 1978. Molecular diffusivities of $\rm H_2^{16}O$, $\rm HD^{16}O$, and $\rm H_2^{18}O$ in gases. J. Chem. Phys. 69 (6), 2864–2871. https://doi.org/10.1063/1.436884.
- Newman, B.D., Wilcox, B.P., Archer, S.R., Breshears, D.D., Dahm, C.N., Duffy, C.J., McDowell, N.G., Phillips, F.M., Scanlon, B.R., Vivoni, E.R., 2006. Ecohydrology of water-limited environments: a scientific vision. Water Resour. Res. 42, W06302. https://doi.org/10.1029/2005WR004141.

- Nippert, J.B., Wieme, R.A., Ocheltree, T.W., Craine, J.M., 2012. Root characteristics of C₄ grasses limit reliance on deep soil water in tallgrass prairie. Plant Soil 355 (1–2), 385–394. https://doi.org/10.1007/s11104-011-1112-4.
- Oerter, E.J., Bowen, G.J., 2019. Spatio-temporal heterogeneity in soil water stable isotopic composition and its ecohydrologic implications in semiarid ecosystems. Hydrol. Proc. 33 (12), 1724–1738. https://doi.org/10.1002/hyp.13434.
- Oerter, E.J., Perelet, A., Pardyjak, E., Bowen, G., 2017. Membrane inlet laser spectroscopy to measure H and O stable isotope compositions of soil and sediment pore water with high sample throughput. Rapid Commun. Mass Sp. 31 (1), 75–84. https://doi.org/10.1002/rcm.7768.
- Penna, D., Hopp, L., Scandellari, F., Allen, S.T., Benettin, P., Beyer, M., Geris, J., Klaus, J., Marshall, J.D., Schwendenmann, L., Volkmann, T.H.M., von Freyberg, J., Amin, A., Ceperley, N., Engel, M., Frentress, J., Giambastiani, Y., McDonnell, J.J., Zuecco, G., Llorens, P., Siegwolf, R.T.W., Dawson, T.E., Kirchner, J.W., 2018. Ideas and perspectives: Tracing terrestrial ecosystem water fluxes using hydrogen and oxygen stable isotopes challenges and opportunities from an interdisciplinary perspective. Biogeosciences 15 (21), 6399–6415. https://doi.org/10.5194/bg-15-6399-2018.
- Phillips, D.L., Gregg, J.W., 2001. Uncertainty in source partitioning using stable isotopes. Oecologia 127 (2), 171–179. https://doi.org/10.1007/s004420000578.
- Quade, M., Klosterhalfen, A., Graf, A., Brüggemann, N., Hermes, N., Vereecken, H., Rothfuss, Y., 2019. In-situ monitoring of soil water isotopic composition for partitioning of evapotranspiration during one growing season of sugar beet (Beta vulgaris). Agric. For. Meteorol. 266-267, 53–64. https://doi.org/10.1016/j. agrformet.2018.12.002.
- Raz-Yaseef, N., Billesbach, D.P., Fischer, M.L., Biraud, S.C., Gunter, S.A., Bradford, J.A., Torn, M.S., 2015. Vulnerability of crops and native grasses to summer drying in the U.S. Southern Great Plains. Agric. Ecosyst. Environ. 213, 209–218. https://doi.org/ 10.1016/j.agee.2015.07.021.
- Riley, W.J., Still, C.J., Helliker, B.R., Ribas-Carbo, M., Berry, J.A., 2003. ¹⁸O composition of CO₂ and H₂O ecosystem pools and fluxes in a tallgrass prairie: Simulations and comparisons to measurements. Global Change Biol. 9 (11), 1567–1581. https://doi.org/10.1046/j.1365-2486.2003.00680.x.
- Risi, C., Landais, A., Bony, S., Jouzel, J., Masson-Delmotte, V., Vimeux, F., 2010.
 Understanding the ¹⁷O excess glacial-interglacial variations in Vostok precipitation.
 J. Geophys. Res. 115 (D10) https://doi.org/10.1029/2008JD011535.
- Rothfuss, Y., Javaux, M., 2017. Reviews and syntheses: Isotopic approaches to quantify root water uptake: a review and comparison of methods. Biogeosciences 14 (8), 2199–2224. https://doi.org/10.5194/bg-14-2199-2017.
- Rothfuss, Y., Vereecken, H., Bruggemann, N., 2013. Monitoring water stable isotopic composition in soils using gas-permeable tubing and infrared laser absorption spectroscopy. Water Resour. Res. 49 (6), 3747–3755. https://doi.org/10.1002/ wrcr.20311.
- Sala, O.E., Gherardi, L.A., Peters, D.P.C., 2015. Enhanced precipitation variability effects on water losses and ecosystem functioning: differential response of arid and mesic regions. Clim. Change 131 (2), 213–227. https://doi.org/10.1007/s10584-015-1380-7
- Samson, F.B., Knopf, F.L., Ostlie, W.R., 2004. Great Plains ecosystems: past, present, and future. Wildlife Society Bulletin, 32. The Wildlife Society, pp. 6–15. https://doi.org/ 10.2193/0091-7648(2004)32[6:GPEPPA12.0.CO:2.
- Scanlon, T.M., Kustas, W.P., 2010. Partitioning carbon dioxide and water vapor fluxes using correlation analysis. Agric. For. Meteorol. 150 (1), 89–99. https://doi.org/ 10.1016/j.agrformet.2009.09.005.
- Schaap, M.G., Leij, F.J., van Genuchten, M.T., 2001. ROSETTA: a computer program for estimating soil hydraulic parameters with hierarchical pedotransfer functions. J. Hydrol. 251 (3), 163–176. https://doi.org/10.1016/S0022-1694(01)00466-8.
- Schlesinger, W.H., Jasechko, S., 2014. Transpiration in the global water cycle. Agric. For. Meteorol. 189-190, 115–117. https://doi.org/10.1016/j.agrformet.2014.01.011.
 Schmidt, M., Maseyk, K., Lett, C., Biron, P., Richard, P., Bariac, T., Seibt, U., 2010.
- Schmidt, M., Maseyk, K., Lett, C., Biron, P., Richard, P., Bariac, T., Seibt, U., 2010. Concentration effects on laser-based δ¹⁸O and δ²H measurements and implications for the calibration of vapour measurements with liquid standards. Rapid Commun. Mass Sp. 24 (24), 3553–3561. https://doi.org/10.1002/rcm.4813.
- Shafer, M., Ojima, D., Antle, J.M., Kluck, D., McPherson, R.A., Petersen, S., Scanlon, B., Sherman, K., 2014. Ch. 19: Great Plains. Climate Change Impacts in the United States: The Third National Climate Assessment. In: Melillo, J.W., Terese, Terese (T. C.), Yohe, G.W. (Eds.), U.S. Global Change Research Program, pp. 441–461. https://doi.org/10.7930/J0D798BC.
- Soderberg, K., Good, S.P., Wang, L.X., Caylor, K., 2012. Stable isotopes of water vapor in the vadose zone: a review of measurement and modeling techniques. Vadose Zone J. 11 (3) https://doi.org/10.2136/vzj2011.0165.
- Sprenger, M., Herbstritt, B., Weiler, M., 2015. Established methods and new opportunities for pore water stable isotope analysis. Hydrol. Proc. 29 (25), 5174–5192. https://doi.org/10.1002/hyp.10643.
- Sprenger, M., Tetzlaff, D., Soulsby, C., 2017. Soil water stable isotopes reveal evaporation dynamics at the soil–plant-atmosphere interface of the critical zone. Hydrol. Earth Syst. Sci. 21 (7), 3839–3858. https://doi.org/10.5194/hess-21-3839-2017.
- Steinauer, E.M., Collins, S.L., 1996. Prairie ecology—The tallgrass prairie. Prairie conservation: preserving North America's most endangered ecosystem. Prairie Conservation. Island Press, Washington, pp. 39–52.
- Sturm, P., Knohl, A., 2010. Water vapor δ²H and δ¹⁸O measurements using off-axis integrated cavity output spectroscopy. Astron. Astrophys. 3 (1), 67–77. https://doi.org/10.5194/amt-3-67-2010.
- Sun, X., Zou, C.B., Wilcox, B., Stebler, E., 2019a. Effect of vegetation on the energy balance and evapotranspiration in tallgrass prairie: a paired study using the eddycovariance method. Boundary-Layer Meteorol. 170 (1), 127–160. https://doi.org/ 10.1007/s10546-018-0388-9.

- Sun, X., Wilcox, B.P., Zou, C.B., 2019b. Evapotranspiration partitioning in dryland ecosystems: a global meta-analysis of in situ studies. J. Hydrol. 576, 123–136. https://doi.org/10.1016/j.jhydrol.2019.06.022.
- Sutanto, S.J., van den Hurk, B., Dirmeyer, P.A., Seneviratne, S.I., Röckmann, T., Trenberth, K.E., Blyth, E.M., Wenninger, J., Hoffmann, G., 2014. HESS Opinions "A perspective on isotope versus non-isotope approaches to determine the contribution of transpiration to total evaporation". Hydrol. Earth Syst. Sci. 18 (8), 2815–2827. https://doi.org/10.5194/hess-18-2815-2014.
- Tetens, O., 1930. Uber einige meteorologische begriffe. Z. Geophys. 6, 297-309.
- Vicente-Serrano, S.M., Gouveia, C., Camarero, J.J., Beguería, S., Trigo, R., López-Moreno, J.I., Azorín-Molina, C., Pasho, E., Lorenzo-Lacruz, J., Revuelto, J., Morán-Tejeda, E., Sanchez-Lorenzo, A., 2013. Response of vegetation to drought time-scales across global land biomes. Proc. Natl. Acad. Sci. 110 (1), 52–57. https://doi.org/10.1073/pnas.1207068110.
- Volkmann, T.H.M., Haberer, K., Gessler, A., Weiler, M., 2016. High-resolution isotope measurements resolve rapid ecohydrological dynamics at the soil–plant interface. New Phytol. 210 (3), 839–849. https://doi.org/10.1111/nph.13868.
- Volkmann, T.H.M., Weiler, M., 2014. Continual in situ monitoring of pore water stable isotopes in the subsurface. Hydrol. Earth Syst. Sci. 18 (5), 1819–1833. https://doi. org/10.5194/hess-18-1819-2014.
- Wagle, P., Xiao, X., Gowda, P., Basara, J., Brunsell, N., Steiner, J., K.C, A., 2017. Analysis and estimation of tallgrass prairie evapotranspiration in the central United States. Agric. For. Meteorol. 232, 35–47. https://doi.org/10.1016/j. agrformet.2016.08.005.
- Wang, L., Niu, S., Good, S.P., Soderberg, K., McCabe, M.F., Sherry, R.A., Luo, Y., Zhou, X., Xia, J., Caylor, K.K., 2013. The effect of warming on grassland evapotranspiration partitioning using laser-based isotope monitoring techniques. Geochim. Cosmochim. Ac. 111, 28–38. https://doi.org/10.1016/j.gca.2012.12.047
- Wang, L.X., Caylor, K.K., Villegas, J.C., Barron-Gafford, G.A., Breshears, D.D., Huxman, T.E., 2010. Partitioning evapotranspiration across gradients of woody plant cover: assessment of a stable isotope technique. Geophys. Res. Lett. 37 (9), L09401. https://doi.org/10.1029/2010GL043228.
- Wang, P., Li, X., Wang, L., Wu, X., Hu, X., Fan, Y., Tong, Y., 2018. Divergent evapotranspiration partition dynamics between shrubs and grasses in a shrubencroached steppe ecosystem. New Phytol. 219 (4), 1325–1337. https://doi.org/ 10.1111/nph.15237.
- Wang, P., Yamanaka, T., Li, X.Y., Wei, Z.W., 2015. Partitioning evapotranspiration in a temperate grassland ecosystem: Numerical modeling with isotopic tracers. Agric. For. Meteorol. 208, 16–31. https://doi.org/10.1016/j.agrformet.2015.04.006.
- Wang, X.F., Yakir, D., 2000. Using stable isotopes of water in evapotranspiration studies. Hydrol. Proc. 14 (8), 1407–1421. https://doi.org/10.1002/1099-1085(20000615) 14:8<1407::AID-HYP992>3.0.CO;2-K.
- Wei, Z., Yoshimura, K., Okazaki, A., Kim, W., Liu, Z., Yokoi, M., 2015. Partitioning of evapotranspiration using high-frequency water vapor isotopic measurement over a rice paddy field. Water Resour. Res. 51 (5), 3716–3729. https://doi.org/10.1002/ 2014/WP016737.
- Welp, L.R., Lee, X., Kim, K., Griffis, T.J., Billmark, K.A., Baker, J.M., 2008. δ¹⁸O of water vapour, evapotranspiration and the sites of leaf water evaporation in a soybean canopy. Plant Cell Environ. 31 (9), 1214–1228. https://doi.org/10.1111/j.1365-3040.2008.01826.x
- Wen, X., Lee, X., Sun, X., Wang, J., Tang, Y., Li, S., Yu, G., 2012. Intercomparison of four commercial analyzers for water vapor isotope measurement. J. Atmos. OceanTechnol. 29 (2), 235–247. https://doi.org/10.1175/JTECH-D-10-05037.1.
- Wen, X., Yang, B., Sun, X., Lee, X., 2016. Evapotran piration partitioning through in-situ oxygen isotope measurements in an oasis cropland. Agric. For. Meteorol. 230-231, 89–96. https://doi.org/10.1016/j.agrformet.2015.12.003.
- West, A.G., Goldsmith, G.R., Brooks, P.D., Dawson, T.E., 2010. Discrepancies between isotope ratio infrared spectroscopy and isotope ratio mass spectrometry for the stable isotope analysis of plant and soil waters. Rapid Commun. Mass Sp. 24 (14), 1948–1954. https://doi.org/10.1002/rcm.4597.
- West, A.G., Goldsmith, G.R., Matimati, I., Dawson, T.E., 2011. Spectral analysis software improves confidence in plant and soil water stable isotope analyses performed by isotope ratio infrared spectroscopy (IRIS). Rapid Commun. Mass Sp. 25 (16), 2268–2274. https://doi.org/10.1002/rcm.5126.
- West, A.G., Patrickson, S.J., Ehleringer, J.R., 2006. Water extraction times for plant and soil materials used in stable isotope analysis. Rapid Commun. Mass Sp. 20 (8), 1317–1321. https://doi.org/10.1002/rcm.2456.
- Williams, D.G., Cable, W., Hultine, K., Hoedjes, J.C.B., Yepez, E.A., Simonneaux, V., Er-Raki, S., Boulet, G., de Bruin, H.A.R., Chehbouni, A., Hartogensis, O.K., Timouk, F., 2004. Evapotranspiration components determined by stable isotope, sap flow and eddy covariance techniques. Agric. For. Meteorol. 125 (3–4), 241–258. https://doi.org/10.1016/j.agrformet.2004.04.008.
- Wu, Y., Du, T., Ding, R., Tong, L., Li, S., Wang, L., 2017. Multiple methods to partition evapotranspiration in a maize field. J. Hydrometeorol. 18 (1), 139–149. https://doi. org/10.1175/JHM-D-16-0138.1.
- Wythers, K.R., Lauenroth, W.K., Paruelo, J.M., 1999. Bare-soil evaporation under semiarid field conditions. Soil Sci. Soc. Am. J. 63 (5), 1341–1349. https://doi.org/ 10.2136/sssaj1999.6351341x.
- Xiao, W., Wei, Z., Wen, X., 2018. Evapotranspiration partitioning at the ecosystem scale using the stable isotope method—a review. Agric. For. Meteorol. 263, 346–361. https://doi.org/10.1016/j.agrformet.2018.09.005.
- Xu, Z., Yang, H., Liu, F., An, S., Cui, J., Wang, Z., Liu, S., 2008. Partitioning evapotranspiration flux components in a subalpine shrubland based on stable isotopic measurements. Bot. Stud. 49 (4), 351–361.
- Yakir, D., Sternberg, L.D.L., 2000. The use of stable isotopes to study ecosystem gas exchange. Oecologia 123 (3), 297–311. https://doi.org/10.1007/s004420051016.

- Yang, B., Wang, P., You, D., Liu, W., 2018. Coupling evapotranspiration partitioning with root water uptake to identify the water consumption characteristics of winter wheat: a case study in the North China Plain. Agric. For. Meteorol. 259, 296–304. https://doi.org/10.1016/j.agrformet.2018.05.017.
- Yepez, E.A., Huxman, T.E., Ignace, D.D., English, N.B., Weltzin, J.F., Castellanos, A.E., Williams, D.G., 2005. Dynamics of transpiration and evaporation following a moisture pulse in semiarid grassland: a chamber-based isotope method for partitioning flux components. Agric. For. Meteorol. 132 (3–4), 359–376. https://doi.org/10.1016/j.agrformet.2005.09.006.
- Yepez, E.A., Williams, D.G., Scott, R.L., Lin, G.H., 2003. Partitioning overstory and understory evapotranspiration in a semiarid savanna woodland from the isotopic composition of water vapor. Agric. For. Meteorol. 119 (1–2), 53–68. https://doi.org/ 10.1016/S0168-1923(03)00116-3.
- Zhang, S., Wen, X., Wang, J., Yu, G., Sun, X., 2010. The use of stable isotopes to partition evapotranspiration fluxes into evaporation and transpiration. Acta Ecologica Sinica 30 (4), 201–209. https://doi.org/10.1016/j.chnaes.2010.06.003.
- Zhang, S., Zhang, J., Liu, B., Zhang, W., Gong, C., Jiang, M., Lv, X., 2018. Evapotranspiration partitioning using a simple isotope-based model in a semiarid marsh wetland in northeastern China. Hydrol. Proc. 32 (4), 493–506. https://doi.org/10.1002/hyp.11430.
- Zhou, S., Yu, B., Zhang, Y., Huang, Y., Wang, G., 2016. Partitioning evapotranspiration based on the concept of underlying water use efficiency. Water Resour. Res. 52 (2), 1160–1175. https://doi.org/10.1002/2015WR017766.
- Zou, C.B., Turton, D.J., Will, R.E., Engle, D.M., Fuhlendorf, S.D., 2014. Alteration of hydrological processes and streamflow with juniper (Juniperus virginiana) encroachment in a mesic grassland catchment. Hydrol. Proc. 28 (26), 6173–6182. https://doi.org/10.1002/hyp.10102.